Comput. Methods Appl. Mech. Engrg. 198 (2009) 2272–2285

Contents lists available at ScienceDirect

Comput. Methods Appl. Mech. Engrg.

journal homepage: www.elsevier.com/locate/cma

Finite element response sensitivity analysis of multi-yield-surface J_2 plasticity model by direct differentiation method

Quan Gu [a], Joel P. Conte [b,*], Ahmed Elgamal [b], Zhaohui Yang [c]

[a] AMEC Geomatrix Consultants Inc., 510 Superior Avenue, Suite 200, Newport Beach, CA 92663, USA
[b] Department of Structural Engineering, University of California at San Diego, 9500 Gilman Drive, La Jolla, CA 92093, USA
[c] URS Corporation, 1333 Broadway, Suite 800, Oakland, CA, USA

ARTICLE INFO

Article history:
Received 11 August 2008
Received in revised form 22 January 2009
Accepted 9 February 2009
Available online 28 February 2009

Keywords:
Nonlinear finite element analysis
Response sensitivity analysis
Multi-yield-surface plasticity model
Direct differentiation method
Soil material model

ABSTRACT

Finite element (FE) response sensitivity analysis is an essential tool for gradient-based optimization methods used in various sub-fields of civil engineering such as structural optimization, reliability analysis, system identification, and finite element model updating. Furthermore, stand-alone sensitivity analysis is invaluable for gaining insight into the effects and relative importance of various system and loading parameters on system response. The direct differentiation method (DDM) is a general, accurate and efficient method to compute FE response sensitivities to FE model parameters. In this paper, the DDM-based response sensitivity analysis methodology is applied to a pressure independent multi-yield-surface J_2 plasticity material model, which has been used extensively to simulate the nonlinear undrained shear behavior of cohesive soils subjected to static and dynamic loading conditions. The complete derivation of the DDM-based response sensitivity algorithm is presented. This algorithm is implemented in a general-purpose nonlinear finite element analysis program. The work presented in this paper extends significantly the framework of DDM-based response sensitivity analysis, since it enables numerous applications involving the use of the multi-yield-surface J_2 plasticity material model. The new algorithm and its software implementation are validated through two application examples, in which DDM-based response sensitivities are compared with their counterparts obtained using forward finite difference (FFD) analysis. The normalized response sensitivity analysis results are then used to measure the relative importance of the soil constitutive parameters on the system response.

1. Introduction

Finite element (FE) response sensitivities represent an essential ingredient for gradient-based optimization methods required in various sub-fields of structural and geotechnical engineering such as structural optimization, reliability analysis, system identification, and FE model updating [1,2]. In addition, FE response sensitivities are invaluable for gaining insight into the effects and relative importance of system and loading parameters in regards to system response.

Several methods are available for response sensitivity computation, including the finite difference method (FDM), the adjoint method (AM), the perturbation method (PM), and the direct differentiation method (DDM). These methods are described by Zhang and Der Kiureghian [3], Kleiber et al. [2], Conte et al. [4–6], Gu and Conte [7], Scott et al. [8], and Haukaas and Der Kiureghian [9]. The FDM is the simplest method for response sensitivity computation, but is computationally expensive and can be negatively affected by numerical noise (i.e., truncation and round-off errors). The AM is extremely efficient for linear and nonlinear elastic systems, but is not a competitive method for path-dependent (i.e., inelastic) problems. The PM is computationally efficient, but generally not very accurate. The DDM, on the other hand, is general, accurate and efficient and is applicable to any material constitutive model (both path-independent and path-dependent). The computation of FE response sensitivities to system and loading parameters based on the DDM requires extension of the FE algorithms for response-only computation [5].

Based on DDM, this paper presents a derivation of response sensitivities with respect to material parameters of an existing material model, the multi-yield-surface J_2 plasticity model. This model was first developed by Iwan [10] and Mroz [11], then applied by Prevost [12–14] to soil mechanics. It was later modified and implemented in OpenSees [15–17] by Yang [18] and Elgamal et al. [19]. OpenSees is an open source software framework for advanced modeling and simulation of structural and geotechnical systems developed under the auspice of the Pacific Earthquake Engineering Research (PEER) Center. In contrast to the classical J_2 (or Von Mises) elasto-plastic behavior with a single yield surface,

* Corresponding author. Tel.: +1 858 822 4545; fax: +1 858 822 2260.
E-mail address: jpconte@ucsd.edu (J.P. Conte).

0045-7825/$ - see front matter © 2009 Elsevier B.V. All rights reserved.
doi:10.1016/j.cma.2009.02.030

multi-yield-surface J_2 plasticity employs the concept of a field of plastic moduli [12–14] to achieve a piecewise linear elasto-plastic behavior under cyclic loading conditions. This field is defined by a collection of nested yield surfaces of constant size (i.e., no isotropic hardening) in the stress space, which define the regions of constant plastic shear moduli (and therefore constant tangent shear moduli). The stress sensitivity to material parameters is computed by differentiating consistently the constitutive law integration algorithm, adding the contributions from all yield surfaces that affect the stress computation at the current time step.

The existing implementation in OpenSees [15] of the multi-yield-surface J_2 plasticity model [18,19] considered is then extended to enable response sensitivity computation using the DDM-based algorithm developed in this paper. The DDM-based algorithm was implemented in OpenSees by extending the existing framework for sensitivity and reliability analysis developed by Der Kiureghian et al. [20], Haukaas and Der Kiureghian [21], and Scott and Haukaas [22].

The work presented in this paper extends significantly the framework of DDM-based response sensitivity analysis, since it enables numerous applications involving the use of the multi-yield-surface J_2 plasticity material model. Although this material model is a rather old model, it remains an effective and robust model to simulate the undrained response of cohesive materials under cyclic and seismic loading conditions [12–14,16,18,19,23–26]. Also, it is operational in OpenSees [18] through which soil–structure-interaction studies may be conducted by a large user community. Thus, an area of application of the present DDM-based FE response sensitivity analysis scheme is in earthquake loading (undrained) for geotechnical cohesive soils, with applications to soil-foundation-structure interaction scenarios [16,17]. Response sensitivity analysis results are needed as input for reliability, optimization, and FE model updating applications. Therefore, the contribution of this paper potentially improves significantly the computational efficiency of such applications to a wide class of geotechnical systems [27–29] and soil-foundation-structure interaction systems involving the dynamic undrained shear response of cohesive soils.

The developments presented in this paper include new implementation details of the DDM that can carry over to other advanced constitutive models. (1) To the authors' knowledge, in past work, the DDM-based response sensitivity analysis methodology has been implemented for uniaxial material constitutive models [2,5,6,8] and three-dimensional (3D) single surface J_2 plasticity models [2,3] with implicit constitutive law integration schemes. In this paper, the DDM methodology is extended to a general 3D elasto-plastic material constitutive model, in which the multi-yield-surface J_2 plasticity approach is utilized. (2) In this plasticity model, the stress state at the current load/time step is obtained through an explicit corrective iteration scheme, which accumulates contributions from all yield surfaces involved, the number of which varies from load/time step to load/ time step [30]. The DDM-based response sensitivity algorithm follows exactly the corrective iteration process for stress computation. (3) The computation of the DDM-based FE response sensitivity requires the consistent and not the continuum tangent material moduli [5]. The consistent tangent moduli consist of an unsymmetrical fourth-order tensor (exhibiting only minor symmetries, $D_{ijkl} = D_{jikl} = D_{jilk} = D_{jilk}$, but $D_{ijkl} \neq D_{klij}$). They are computed by differentiating the stress tensor with respect to the strain tensor by following exactly the stress computation algorithm as presented in [30]. (4) The sensitivities of the kinematic hardening parameters defining the initial configuration of the multi-yield surfaces are required at the initiation of the response and response sensitivity computation. Furthermore, the sensitivities of the kinematic hardening parameters defining the active and inner yield surfaces must be updated at each load/time step.

Two application examples are provided to validate the new response sensitivity algorithm and its implementation using the finite difference method (FDM). As an application of response sensitivity analysis, the response sensitivity results are used to measure the relative importance of the soil material parameters of different soil layers on the displacement response of the soil.

2. Constitutive formulation of multi-yield-surface J_2 plasticity model and numerical integration

2.1. Multi-yield surfaces

Each yield surface of this multi-yield-surface J_2 plasticity model is defined in the deviatoric stress space as [23]

$$f = \left\{\frac{3}{2}((\boldsymbol{\tau}-\boldsymbol{\alpha}):(\boldsymbol{\tau}-\boldsymbol{\alpha}))\right\}^{\frac{1}{2}} - K = 0, \tag{1}$$

where $\boldsymbol{\tau}$ denotes the deviatoric stress tensor and $\boldsymbol{\alpha}$, referred to as back-stress tensor, denotes the center of the yield surface $\{f = 0\}$ in the deviatoric stress space. Parameter K represents the size ($\sqrt{3/2}$ times the radius) of the yield surface which defines the region of constant plastic shear modulus. The dyadic tensor product of tensors $\mathbf{A}$ and $\mathbf{B}$ is defined as $\mathbf{A}:\mathbf{B} = A_{ij}B_{ij}$ ($i, j = 1, 2, 3$). The back-stress $\boldsymbol{\alpha}$ is initialized to zero at the start of loading.

In geotechnical engineering, the nonlinear shear behavior of soil materials is described by a shear stress–strain backbone curve [18,19] as shown in Fig. 1a. The experimentally determined backbone curve can be approximated by the hyperbolic formula [31] as

$$\tau = \frac{G\gamma}{1 + (\gamma/\gamma_r)}, \tag{2}$$

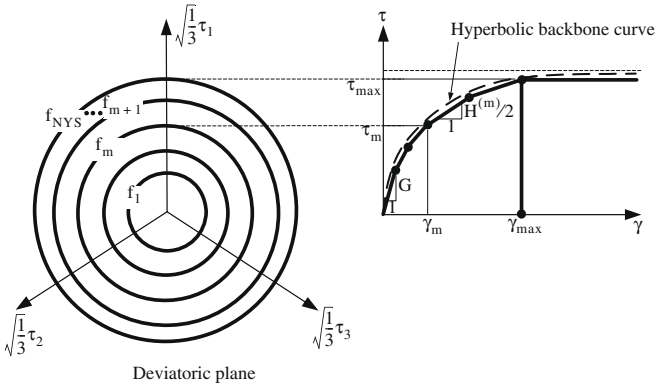

(a) Octahedral shear stress-strain (after [12])

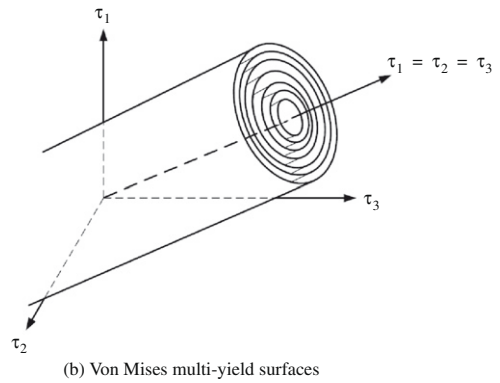

(b) Von Mises multi-yield surfaces

Fig. 1. Yield surfaces of multi-yield-surface J_2 plasticity model in principal deviatoric stress space.

where τ and γ denote the octahedral shear stress and shear strain, respectively, and G is the low-strain shear modulus. Parameter γ_r is a reference shear strain defined as

$$\gamma_r = \frac{\gamma_{\max}\tau_{\max}}{G\gamma_{\max} - \tau_{\max}}, \tag{3}$$

where $\tau_{\max}$, called shear strength, is the shear stress corresponding to the shear strain $\gamma = \gamma_{\max}$ (selected sufficiently large so that $\tau_{\max} \approx \tau(\gamma = \infty)$) (see Fig. 1).

Within the framework of multi-yield-surface plasticity, the hyperbolic backbone curve in Eq. (2) is replaced by a piecewise linear approximation as shown in Fig. 1a. Each line segment represents the domain of a yield surface $\{f_i = 0\}$ of size $K^{(i)}$ characterized by an elasto-plastic shear modulus $H^{(i)}$ for $i = 1, 2, \ldots,$ NYS, where NYS denotes the total number of yield surfaces [12–14]. Parameter $H^{(i)}$ (see Fig. 1a) is conveniently defined as $H^{(i)} = 2\left(\frac{\tau_{i+1}-\tau_i}{\gamma_{i+1}-\gamma_i}\right)$. A constant plastic shear modulus $H'^{(i)}$ defined as [32]

$$\frac{1}{H'^{(i)}} = \frac{1}{H^{(i)}} - \frac{1}{2G} \tag{4}$$

is associated with each yield surface $\{f_i = 0\}$.

The stress–strain points (τ_j, γ_j) (subscript j denotes the point number) used to define the piecewise linear approximation of the shear stress–strain $(\tau - \gamma)$ backbone curve are defined such that their projections on the τ axis are uniformly spaced (see Fig. 1). Thus,

$$\tau_j = \tau_{\max}\frac{j}{\text{NYS}} \quad \text{and} \quad \gamma_j = \frac{\tau_j\gamma_r}{G\gamma_r - \tau_j} \quad (j = 1, 2, \ldots, \text{NYS} - 1). \tag{5}$$

The j-th yield surface $\{f_j = 0\}$ is defined by the two points (τ_j, γ_j) and $(\tau_{j+1}, \gamma_{j+1})$ (see Fig. 1). For each yield surface j with $1 \leqslant j \leqslant \text{NYS} - 1$,

$$(\Delta\gamma)_j = \gamma_{j+1} - \gamma_j, \tag{6}$$

$$(\Delta\tau)_j = \tau_{j+1} - \tau_j, \tag{7}$$

$$K^{(j)} = \frac{3}{\sqrt{2}}\tau_j, \tag{8}$$

$$H^{(j)} = \frac{2(\Delta\tau)_j}{(\Delta\gamma)_j}, \tag{9}$$

$$H'^{(j)} = \frac{2GH^{(j)}}{2G - H^{(j)}}. \tag{10}$$

For the outermost yield surface (failure surface), set $H^{(\text{NYS})} = H'^{(\text{NYS})} = 0$. The yield surfaces in their initial positions (at the start of loading) represent a set of concentric cylindrical surfaces whose axes coincide with the hydrostatic axis in the deviatoric stress space as shown in Fig. 1b. The outermost yield surface $\{f_{\text{NYS}} = 0\}$ represents a failure surface and therefore defines a geometrical boundary in the deviatoric stress space.

It is worth mentioning that the yield surfaces may initially be configured any way suggested by experimental data and typically would not be concentric if calibration is based on triaxial test data for instance.

2.2. Flow rule

An associative flow rule is used to compute the plastic strain increments. In the deviatoric stress space, the plastic strain increment vector lies along the exterior normal to the yield surface at the stress point. In tensor notation, the plastic strain increment is expressed as

$$d\epsilon^{\text{p}} = \frac{\langle L\rangle}{H'}\mathbf{Q}, \tag{11}$$

where the second-order unit tensor $\mathbf{Q}$ defined as

$$\mathbf{Q} = \frac{1}{Q}\frac{\partial f}{\partial \boldsymbol{\sigma}} \tag{12}$$

in which $Q = \left\{\frac{\partial f}{\partial \boldsymbol{\sigma}} : \frac{\partial f}{\partial \boldsymbol{\sigma}}\right\}^{\frac{1}{2}}$, represents the plastic flow direction normal to the yield surface face $\{f = 0\}$ at the current stress point. Parameter L in Eq. (11), referred to as the plastic loading function, is defined as the projection of the stress increment vector $d\tau$ onto the direction normal to the yield surface, i.e.,

$$L = \mathbf{Q} : d\boldsymbol{\tau}. \tag{13}$$

The symbol $\langle\rangle$ in Eq. (11) denotes the MacCauley's brackets defined such that $\langle L\rangle = \max(L, 0)$. The magnitude of the plastic strain increment, $\frac{\langle L\rangle}{H'}$, is a non-negative function which obeys the Kuhn-Tucker complementarity conditions expressed as $\frac{\langle L\rangle}{H'}f(\boldsymbol{\tau}, \boldsymbol{\alpha}) = 0$, such that the plastic strain increment is zero in the elastic case (i.e., when $f(\boldsymbol{\tau}, \boldsymbol{\alpha}) < 0$).

The flow rule defined above in differential (continuum) form is integrated numerically over a trial time step (or load step) using an elastic predictor-plastic corrector procedure illustrated in Fig. 2, which shows, as an illustration, two corrective iterations before convergence is achieved. In this figure, the first subscript n (or $n + 1$) attached to a material response parameter denotes the last (or current) converged load/time step, while the second subscript i indicates the ith corrective iteration (not to be confused with the iteration number of the Newton–Raphson scheme used to solve the nonlinear equilibrium equations at each time step). Assuming that the current active yield surface is the mth surface $\{f_m = 0\}$ with its center at $\boldsymbol{\alpha}_n^{(m)}$, the elastic trial (deviatoric) stress $\boldsymbol{\tau}_{n+1,0}^{\text{tr}}$ is obtained as

$$\boldsymbol{\tau}_{n+1,0}^{\text{tr}} = \boldsymbol{\tau}_n + 2G\Delta\mathbf{e}_{n+1}, \tag{14}$$

where $\boldsymbol{\tau}_n$ is the converged deviatoric stress at the last (nth) time step, and $\Delta\mathbf{e}_{n+1}$ denotes the total (from last converged step) devia-

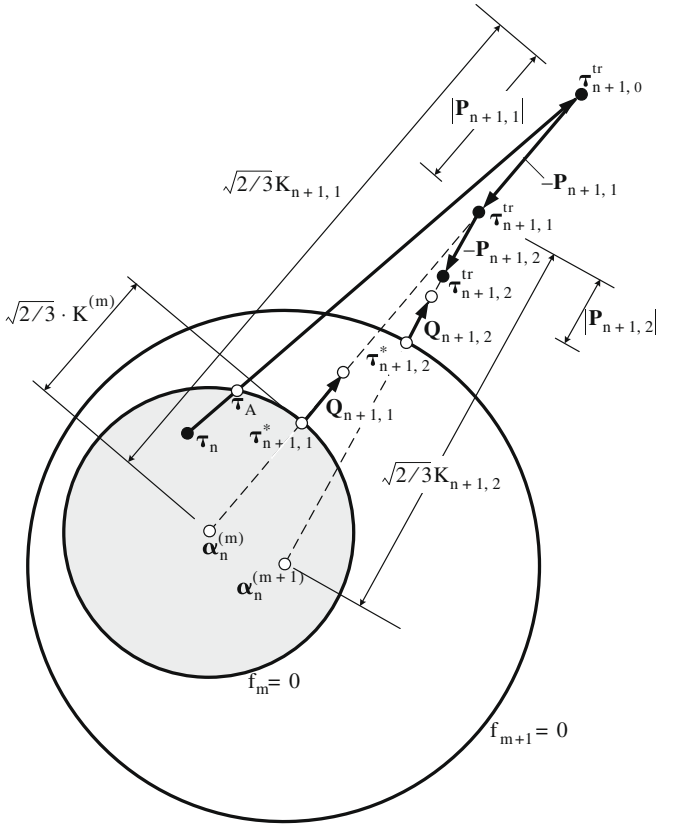

Fig. 2. Schematic of flow rule of multi-yield-surface J_2 plasticity model.

toric strain increment in the current time step. If trial the trial stress $\boldsymbol{\tau}^{\mathrm{tr}}_{n+1,0}$ falls inside the current yield surface $\{f_m = 0\}$, then the iteration process for the integration of the material constitutive law is converged, otherwise a plastic correction (or corrective iteration) is applied as follows. The plastic stress correction tensor $\mathbf{P}_{n+1,i}$ for the current active yield surface ($\{f_m = 0\}$) is defined as (see Fig. 2 for $i = 1$ and 2)

$$\mathbf{P}_{n+1,i} = \boldsymbol{\tau}^{\mathrm{tr}}_{n+1,i-1} - \boldsymbol{\tau}^{\mathrm{tr}}_{n+1,i} \quad (i = 1, 2, 3 \ldots). \tag{15}$$

An important stress quantity called the contact stress $\boldsymbol{\tau}^{*}_{n+1,i}$ is defined as the intersection point of vector $\boldsymbol{\tau}^{\mathrm{tr}}_{n+1,i-1} - \boldsymbol{\alpha}^{(m)}_{n}$ and the current active yield surface $\{f_m = 0\}$, and can be computed as (see Fig. 2 for $i = 1$ and 2)

$$\boldsymbol{\tau}^{*}_{n+1,i} = \frac{K^{(m)}}{K_{n+1,i}} \left(\boldsymbol{\tau}^{\mathrm{tr}}_{n+1,i-1} - \boldsymbol{\alpha}^{(m)}_{n}\right) + \boldsymbol{\alpha}^{(m)}_{n}, \tag{16}$$

where $K_{n+1,i}$ (different from $K^{(i)} = \sqrt{3/2}$ times the radius of the i-th yield surface) is defined as

$$K_{n+1,i} = \sqrt{\frac{3}{2}\left(\boldsymbol{\tau}^{\mathrm{tr}}_{n+1,i-1} - \boldsymbol{\alpha}^{(m)}_{n}\right) : \left(\boldsymbol{\tau}^{\mathrm{tr}}_{n+1,i-1} - \boldsymbol{\alpha}^{(m)}_{n}\right)}, \tag{17}$$

which is $\sqrt{3/2}$ times the distance from $\boldsymbol{\tau}^{t_r}_{n+1,i-1}$ to $\boldsymbol{\alpha}^{(m)}_{n}$. The unit tensor normal to the current active yield surface $\{f_m = 0\}$ at $\boldsymbol{\tau}^{*}_{n+1,i}$ is derived from Eq. (12) or Fig. 2 as

$$\mathbf{Q}_{n+1,i} = \frac{\left(\boldsymbol{\tau}^{*}_{n+1,i} - \boldsymbol{\alpha}^{(m)}_{n}\right)}{\left[\left(\boldsymbol{\tau}^{*}_{n+1,i} - \boldsymbol{\alpha}^{(m)}_{n}\right) : \left(\boldsymbol{\tau}^{*}_{n+1,i} - \boldsymbol{\alpha}^{(m)}_{n}\right)\right]^{\frac{1}{2}}}. \tag{18}$$

The plastic stress correction tensor $\mathbf{P}_{n+1,\,i}$ ($i = 1, 2, 3, \ldots$) can be derived as [32,33]

$$\mathbf{P}_{n+1,1} = 2G \frac{\mathbf{Q}_{n+1,1} : \left(\boldsymbol{\tau}^{\mathrm{tr}}_{n+1,0} - \boldsymbol{\tau}^{*}_{n+1,1}\right)}{\left(H'^{(m)} + 2G\right)} \mathbf{Q}_{n+1,1} \tag{19}$$

and

$$\mathbf{P}_{n+1,i} = 2G \cdot \frac{\mathbf{Q}_{n+1,i} : \left(\boldsymbol{\tau}^{\mathrm{tr}}_{n+1,i-1} - \boldsymbol{\tau}^{*}_{n+1,i}\right)}{\left(H'^{(m)} + 2 \cdot G\right)} \cdot \frac{\left(H'^{(m-1)} - H'^{(m)}\right)}{H'^{(m-1)}} \cdot \mathbf{Q}_{n+1,i} \quad (i = 2, 3, 4, \ldots). \tag{20}$$

The trial stress after the plastic correction for the current active yield surface is obtained using Eq. (15) as

$$\boldsymbol{\tau}^{\mathrm{tr}}_{n+1,i} = \boldsymbol{\tau}^{\mathrm{tr}}_{n+1,i-1} - \mathbf{P}_{n+1,i} \quad (i = 1, 2, 3, \ldots). \tag{21}$$

If the trial stress $\boldsymbol{\tau}^{\mathrm{tr}}_{n+1,i}$ lies outside the next yield surface $\{f_{m+1} = 0\}$, the active yield surface index is set to $m = m + 1$, the corrective iteration number is set to $i = i + 1$ and the plastic correction process (Eqs. (16)–(21)) is repeated until the trial stress $\boldsymbol{\tau}^{\mathrm{tr}}_{n+1,i}$ falls inside the next outer yield surface. After "convergence" of the deviatoric stress $\boldsymbol{\tau}^{\mathrm{tr}}_{n+1,i}$ to $\boldsymbol{\tau}^{\mathrm{tr}}_{n+1}$ is achieved following the above iterative algorithm, the volumetric stress $\sigma^{\mathrm{vol}}_{n+1}$ is updated to

$$\sigma^{\mathrm{vol}}_{n+1} = \sigma^{\mathrm{vol}}_{n} + B(\Delta\boldsymbol{\epsilon}_{n+1} : \mathbf{I}), \tag{22}$$

where B = elastic bulk modulus, $\Delta\boldsymbol{\epsilon}_{n+1}$ = total strain tensor increment, and $\mathbf{I}$ = second order unit tensor. Then, the new total stress (at the end of the integration of the material constitutive law over a trial time/load step) referred to as the current stress point is given by

$$\boldsymbol{\sigma}_{n+1} = \boldsymbol{\tau}_{n+1} + \boldsymbol{\sigma}^{\mathrm{vol}}_{n+1} \cdot \mathbf{I}. \tag{23}$$

2.3. Hardening law

A pure deviatoric kinematic hardening rule is employed to capture the Masing-type hysteretic cyclic response behavior of clays under undrained shear loading conditions [19]. Accordingly, all yield surfaces may translate in the deviatoric stress space to the current stress point without changing in size (i.e., no isotropic hardening). In the context of multi-surface plasticity, translation of the current active yield surface $\{f_m = 0\}$ is generally governed by the consideration that no overlapping is allowed between the current and next yield surfaces [11]. On this basis, the translation direction $\boldsymbol{\mu}_{n+1}$ as shown in Fig. 3 is defined after [19] as

$$\boldsymbol{\mu}_{n+1} = \left[\boldsymbol{\tau}_{\mathrm{T}} - \boldsymbol{\alpha}^{(m)}_{n}\right] - \frac{K^{(m)}}{K^{(m+1)}}\left[\boldsymbol{\tau}_{\mathrm{T}} - \boldsymbol{\alpha}^{(m+1)}_{n}\right], \tag{24}$$

where $\boldsymbol{\tau}_{\mathrm{T}}$ is the deviatoric stress tensor defining the position of stress point T, see Fig. 3, as the intersection of $\{f_{m+1} = 0\}$ (the outer yield surface next to the current active yield surface) with the vector connecting the center $\boldsymbol{\alpha}^{(m)}_{n}$ of the current yield surface and the current stress state ($\boldsymbol{\tau}_{n+1}$) at the end of the trial time/load step. The hardening rule defined in Eq. (24) is also based on Mroz conjugate-points concept [11], and guarantees no overlapping of yield surfaces [19]. Once the translation direction $\boldsymbol{\mu}_{n+1}$ is computed from Eq. (24), the current active yield surface $\{f_m = 0\}$ is translated (or updated) in the direction $\boldsymbol{\mu}_{n+1}$ until it touches the current stress point $\boldsymbol{\tau}_{n+1}$. After the active yield surface ($\{f_m = 0\}$) is updated, all the inner yield surfaces are updated based on the current active yield surface. For the detailed updating process of the active and inner yield surfaces, the following two steps are performed.

2.3.1. Active yield surface update

Compute the deviatoric stress $\boldsymbol{\tau}_{\mathrm{T}}$ (see Fig. 3) as

$$\boldsymbol{\tau}_{\mathrm{T}} = \boldsymbol{\alpha}^{(m)}_{n} + \xi\left(\boldsymbol{\tau}_{n+1} - \boldsymbol{\alpha}^{(m)}_{n}\right), \tag{25}$$

where the unknown scalar parameter ξ is obtained from the condition that $\boldsymbol{\tau}_{\mathrm{T}}$ lies on the yield surface $\{f_{m+1} = 0\}$, i.e., $\boldsymbol{\tau}_{\mathrm{T}}$ has to satisfy

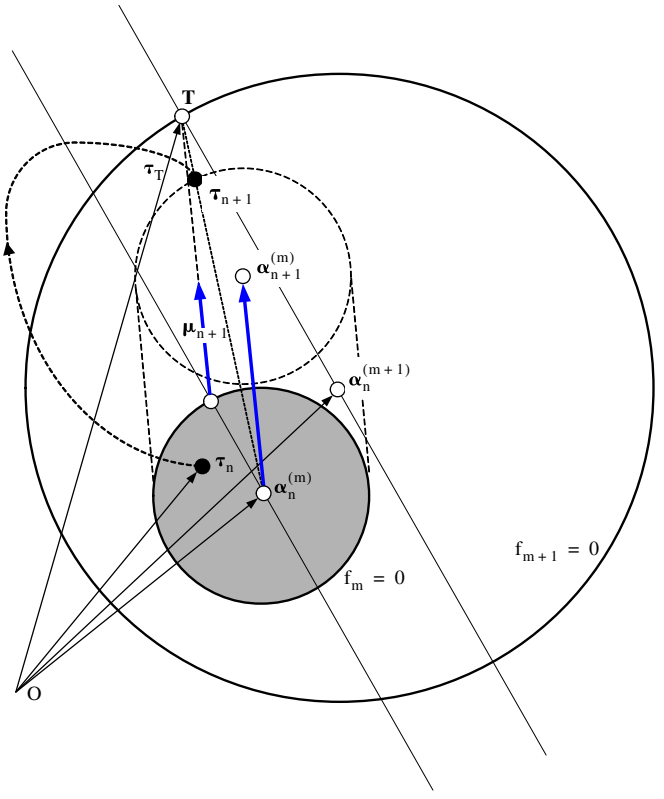

Fig. 3. Hardening rule of multi-yield-surface J_2 plasticity model where $\{f_m = 0\}$ represents the current active yield surface, $\boldsymbol{\tau}_n$ is the converged deviatoric stress at the last time step, and $\boldsymbol{\tau}_{n+1}$ is the current stress at the end of the trial time/load step (after [19]).

$$(\boldsymbol{\tau}_{\mathrm{T}} - \boldsymbol{\alpha}_n^{(m+1)}) : (\boldsymbol{\tau}_{\mathrm{T}} - \boldsymbol{\alpha}_n^{(m+1)}) - \frac{2}{3}(K^{(m+1)})^2 = 0. \tag{26}$$

Substituting Eqs. (25) into (26) yields the following scalar quadratic equation to be solved for parameter ξ:

$$A\xi^2 + B\xi + C = 0, \tag{27}$$

where the coefficients A, B, and C are given by

$$A = (\boldsymbol{\tau}_{n+1} - \boldsymbol{\alpha}_n^{(m)}) : (\boldsymbol{\tau}_{n+1} - \boldsymbol{\alpha}_n^{(m)}), \tag{28}$$

$$B = 2(\boldsymbol{\alpha}_n^{(m)} - \boldsymbol{\alpha}_n^{(m+1)}) : (\boldsymbol{\tau}_{n+1} - \boldsymbol{\alpha}_n^{(m)}), \tag{29}$$

$$C = (\boldsymbol{\alpha}_n^{(m)} - \boldsymbol{\alpha}_n^{(m+1)}) : (\boldsymbol{\alpha}_n^{(m)} - \boldsymbol{\alpha}_n^{(m+1)}) - \frac{2}{3}(K^{(m+1)})^2. \tag{30}$$

From the geometric interpretation of Eq. (25) (see Fig. 3), it follows that Eq. (27) has two real roots of opposite signs. The positive root is the solution retained for ξ. Once $\boldsymbol{\tau}_{\mathrm{T}}$ is known, the translation direction $\boldsymbol{\mu}_{n+1}$ (not necessarily a unit vector) can be computed from Eq. (24). After $\boldsymbol{\mu}_{n+1}$ is obtained, the magnitude of the translation (i.e., $\zeta\boldsymbol{\mu}_{n+1}$ where ζ is a positive scalar to be determined) is computed from the condition that the current stress $\boldsymbol{\tau}_{n+1}$ lies on the mth yield surface $\{f_m = 0\}$ after it is translated. Thus,

$$[\boldsymbol{\tau}_{n+1} - (\boldsymbol{\alpha}_n^{(m)} + \zeta\boldsymbol{\mu}_{n+1})] : [\boldsymbol{\tau}_{n+1} - (\boldsymbol{\alpha}_n^{(m)} + \zeta\boldsymbol{\mu}_{n+1})] - \frac{2}{3}(K^{(m)})^2 = 0, \tag{31}$$

which reduces to the following quadratic equation:

$$A'\zeta^2 + B'\zeta + C' = 0, \tag{32}$$

where the coefficients A', B', and C' are given by

$$A' = \boldsymbol{\mu}_{n+1} : \boldsymbol{\mu}_{n+1}, \tag{33}$$

$$B' = -2\boldsymbol{\mu}_{n+1} : (\boldsymbol{\tau}_{n+1} - \boldsymbol{\alpha}_n^{(m)}), \tag{34}$$

$$C' = (\boldsymbol{\tau}_{n+1} - \boldsymbol{\alpha}_n^{(m)}) : (\boldsymbol{\tau}_{n+1} - \boldsymbol{\alpha}_n^{(m)}) - \frac{2}{3}(K^{(m)})^2. \tag{35}$$

From the geometric interpretation of Eq. (31) (see Fig. 3), it follows that Eq. (32) has two real positive roots. The smaller root is the solution to the problem. After parameter ζ is obtained, the center of the active yield surface $\{f_m = 0\}$ is updated to

$$\boldsymbol{\alpha}_{n+1}^{m} = \boldsymbol{\alpha}_n^{m} + \zeta\boldsymbol{\mu}_{n+1}. \tag{36}$$

2.3.2. Inner yield surface update

After the current active yield surface $\{f_m = 0\}$ is updated, all the inner yield surfaces, $\{f_1 = 0\}$,$\{f_2 = 0\}$,..., and $\{f_{m-1} = 0\}$, are updated such that all yield surfaces $\{f_1 = 0\}$ to $\{f_m = 0\}$ are tangent to each other at the current stress point τ as shown in Fig. 4. The updating of the inner yield surfaces is achieved through similarity as [12]

$$\frac{\boldsymbol{\tau}_{n+1} - \boldsymbol{\alpha}_{n+1}^{(m)}}{K^{(m)}} = \frac{\boldsymbol{\tau}_{n+1} - \boldsymbol{\alpha}_{n+1}^{(m-1)}}{K^{(m-1)}} = \cdots = \frac{\boldsymbol{\tau}_{n+1} - \boldsymbol{\alpha}_{n+1}^{(1)}}{K^{(1)}}. \tag{37}$$

From Eq. (37), the updated center of each of the inner yield surfaces is obtained as

$$\boldsymbol{\alpha}_{n+1}^{(i)} = \boldsymbol{\tau}_{n+1} - \frac{K^{(i)}(\boldsymbol{\tau}_{n+1} - \boldsymbol{\alpha}_{n+1}^{(m)})}{K^{(m)}} \quad (1 \leqslant i \leqslant m-1). \tag{38}$$

3. Derivation of response sensitivity algorithm for multi-yield-surface J_2 plasticity model

3.1. Introduction

If r denotes a generic scalar response quantity (e.g., displacement, strain, stress), then by definition, the sensitivity of r with respect to the (material or loading) parameter θ is expressed mathematically as the absolute partial derivative of r with respect to the variable θ, $\frac{\partial r}{\partial \theta}\big|_{\theta=\theta_0}$, where θ_0 denotes the nominal value taken by the sensitivity parameter θ for the finite element response analysis.

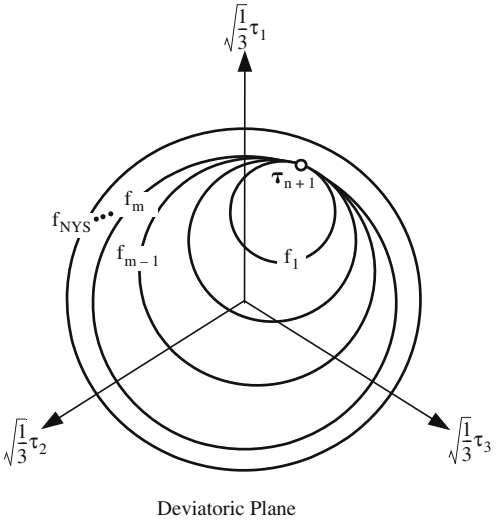

Fig. 4. Inner yield surface movements.

In this paper, following the notation proposed in Ref. [2], the scalar response quantity $r(\boldsymbol{\vartheta}) = r(\mathbf{f}(\boldsymbol{\vartheta}), \boldsymbol{\vartheta})$ depends on the parameter vector $\boldsymbol{\vartheta}$ (defined by n time-independent sensitivity parameters, i.e., $\boldsymbol{\vartheta} = [\theta_1 \cdots \theta_n]^{\mathrm{T}}$) both explicitly and implicitly through the vector function $\mathbf{f}(\boldsymbol{\vartheta})$. According to the notation adopted herein, $\frac{\mathrm{d}r}{\mathrm{d}\boldsymbol{\vartheta}}$ denotes the gradient or total derivative of r with respect to $\boldsymbol{\vartheta}$, $\frac{\mathrm{d}r}{\mathrm{d}\theta_i}$ represents the absolute partial derivative of the response quantity r with respect to the scalar variable θ_i, $i = 1,\ldots,n$, (i.e., the derivative of r with respect to parameter θ_i considering both explicit and implicit dependencies of r on θ_i), and $\frac{\partial r}{\partial \theta_i}\big|_{\mathbf{z}}$ denotes the partial derivative of r with respect to parameter θ_i when the vector of variables $\mathbf{z}$ is kept constant (fixed). In the particular and important case in which $\mathbf{z} = \mathbf{f}(\boldsymbol{\vartheta})$, the expression $\frac{\partial r}{\partial \theta_i}\big|_{\mathbf{z}}$ reduces to the partial derivative of r considering only the explicit dependency of r on parameter θ_i. For $\boldsymbol{\vartheta} = \theta = \theta_1$ (case of a single sensitivity parameter), the adopted notation reduces to the usual elementary calculus notation. The derivations below consider the case of a single (scalar) sensitivity (material or loading) parameter θ without loss of generality, due to the uncoupled nature of the sensitivity equations with respect to different sensitivity parameters.

In the context of nonlinear finite element (FE) response analysis, the consistent FE response sensitivities based on the direct differentiation method (DDM) are computed at each time or load step, after convergence is achieved for the response computation. This requires consistent differentiation of the FE algorithm for the response-only computation (including the numerical integration schemes for the various material constitutive laws used in the FE model) with respect to each sensitivity parameter θ. Consequently, the response sensitivity computation algorithm involves the various hierarchical layers of FE response analysis, namely the: (1) structure/system level, (2) element level, (3) Gauss point level (or section level), and (4) material level. Details on the derivation of the DDM-based sensitivity equations for classical displacement-based, force-based and mixed finite elements can be found in a number of Refs. [4,6–9,20–22,33,34].

3.2. Displacement-based FE response sensitivity analysis using DDM

After spatial discretization using the finite element method, the equations of motion of a materially-nonlinear-only model of a structural system take the form of the following nonlinear matrix differential equation:

$$\mathbf{M}(\theta)\ddot{\mathbf{u}}(t,\theta)+\mathbf{C}(\theta)\dot{\mathbf{u}}(t,\theta)+\mathbf{R}(\mathbf{u}(t,\theta),\theta)=\mathbf{F}(t,\theta), \tag{39}$$

where t = time, θ = scalar sensitivity parameter (material or loading variable), $\mathbf{u}(t)$ = vector of nodal displacements, $\mathbf{M}$ = mass matrix, $\mathbf{C}$ = damping matrix, $\mathbf{R}(\mathbf{u},\ t)$ = history dependent internal (inelastic) resisting force vector, $\mathbf{F}(t)$ = applied dynamic load vector, and a superposed dot denotes one differentiation with respect to time.

We assume without loss of generality that the time continuous spatially discrete equation of motion (39) is integrated numerically in time using the well-known Newmark-β time-stepping method of structural dynamics [35], yielding the following nonlinear matrix algebraic equation in the unknowns $\mathbf{u}_{n+1}=\mathbf{u}(t_{n+1})$:

$$\begin{aligned}\boldsymbol{\Psi}(\mathbf{u}_{n+1})&=\widetilde{\mathbf{F}}_{n+1}-\left[\frac{1}{\beta(\Delta t)^2}\mathbf{M}\mathbf{u}_{n+1}+\frac{\alpha}{\beta(\Delta t)^2}\mathbf{C}\mathbf{u}_{n+1}+\mathbf{R}(\mathbf{u}_{n+1})\right]\\&=\mathbf{0},\end{aligned} \tag{40}$$

where

$$\begin{aligned}\widetilde{\mathbf{F}}_{n+1}=\mathbf{F}_{n+1}&+\mathbf{M}\left[\frac{1}{\beta(\Delta t)^2}\mathbf{u}_n+\frac{1}{\beta(\Delta t)}\dot{\mathbf{u}}_n-\left(1-\frac{1}{2\beta}\right)\ddot{\mathbf{u}}_n\right]\\&+\mathbf{C}\left[\frac{\alpha}{\beta(\Delta t)}\mathbf{u}_n-\left(1-\frac{\alpha}{\beta}\right)\dot{\mathbf{u}}_n-(\Delta t)\left(1-\frac{\alpha}{2\beta}\right)\ddot{\mathbf{u}}_n\right],\end{aligned} \tag{41}$$

α and β are parameters controlling the accuracy and stability of the numerical integration algorithm and Δt is the time integration step assumed to be constant.

Eq. (40) represents the set of nonlinear algebraic equations that have to be solved at each time step $[t_n,\ t_{n+1}]$ for the unknown response quantities $\mathbf{u}_{n+1}$. In general, the subscript $(\ldots)_{n+1}$ indicates that the quantity to which it is attached is evaluated at discrete time t_{n+1}. In the direct stiffness (finite element) method, the vector of internal resisting forces $\mathbf{R}(\mathbf{u}_{n+1})$ in Eq. (40) is obtained by assembling, at the structure level, the elemental internal resisting force vectors, i.e.,

$$\mathbf{R}(\mathbf{u}_{n+1})=\mathop{\mathbf{A}}_{e=1}^{\mathrm{Nel}}\{\mathbf{R}^{(e)}(\mathbf{u}_{n+1}^{(e)})\}, \tag{42}$$

where $\mathbf{A}_{e=1}^{\mathrm{Nel}}\{\ldots\}$ denotes the direct stiffness assembly operator from the element level (in local elements coordinates) to the structure level in global reference coordinates, Nel represents the number of finite elements in the FE model, $\mathbf{R}^{(e)}$ and $\mathbf{u}_{n+1}^{(e)}$ denote the internal resisting force vector and nodal displacement vector, respectively, of element e.

Typically, Eq. (40) is solved using the Newton–Raphson iteration procedure, which consists of solving a linearized system of equations at each iteration. Assuming that $\mathbf{u}_{n+1}$ is the converged solution (up to some iteration residuals satisfying a specified tolerance usually taken in the vicinity of the machine precision) for the current time step $[t_n,\ t_{n+1}]$, and differentiating Eq. (40) with respect to θ using the chain rule, recognizing that $\mathbf{R}(\mathbf{u}_{n+1})=\mathbf{R}(\mathbf{u}_{n+1}(\theta),\ \theta)$ (i.e., the structure inelastic resisting force vector depends on θ both implicitly, through $\mathbf{u}_{n+1}$, and explicitly), we obtain the following response sensitivity equation at the structure level:

$$\begin{aligned}&\left[\frac{1}{\beta(\Delta t)^2}\mathbf{M}+\frac{\alpha}{\beta(\Delta t)}\mathbf{C}+(\mathbf{K}_{\mathrm{T}}^{\mathrm{stat}})_{n+1}\right]\frac{\mathrm{d}\mathbf{u}_{n+1}}{\mathrm{d}\theta}\\&\quad=-\left(\frac{1}{\beta(\Delta t)^2}\frac{\mathrm{d}\mathbf{M}}{\mathrm{d}\theta}+\frac{\alpha}{\beta(\Delta t)}\frac{\mathrm{d}\mathbf{C}}{\mathrm{d}\theta}\right)\mathbf{u}_{n+1}-\left.\frac{\partial\mathbf{R}(\mathbf{u}_{n+1}(\theta),\theta)}{\partial\theta}\right|_{\mathbf{u}_{n+1}}+\frac{\mathrm{d}\widetilde{\mathbf{F}}_{n+1}}{\mathrm{d}\theta},\end{aligned} \tag{43}$$

where

$$\begin{aligned}\frac{\mathrm{d}\widetilde{\mathbf{F}}_{n+1}}{\mathrm{d}\theta}=\frac{\mathrm{d}\mathbf{F}_{n+1}}{\mathrm{d}\theta}&+\frac{\mathrm{d}\mathbf{M}}{\mathrm{d}\theta}\left(\frac{1}{\beta(\Delta t)^2}\mathbf{u}_n+\frac{1}{\beta(\Delta t)}\dot{\mathbf{u}}_n-\left(1-\frac{1}{2\beta}\right)\ddot{\mathbf{u}}_n\right)\\&+\mathbf{M}\left[\frac{1}{\beta(\Delta t)^2}\frac{\mathrm{d}\mathbf{u}_n}{\mathrm{d}\theta}+\frac{1}{\beta(\Delta t)}\frac{\mathrm{d}\dot{\mathbf{u}}_n}{\mathrm{d}\theta}-\left(1-\frac{1}{2\beta}\right)\frac{\mathrm{d}\ddot{\mathbf{u}}_n}{\mathrm{d}\theta}\right]\\&+\frac{\mathrm{d}\mathbf{C}}{\mathrm{d}\theta}\left[\frac{\alpha}{\beta(\Delta t)}\mathbf{u}_n-\left(1-\frac{\alpha}{\beta}\right)\dot{\mathbf{u}}_n-(\Delta t)\left(1-\frac{\alpha}{2\beta}\right)\ddot{\mathbf{u}}_n\right]\\&+\mathbf{C}\left[\frac{\alpha}{\beta(\Delta t)}\frac{\mathrm{d}\mathbf{u}_n}{\mathrm{d}\theta}-\left(1-\frac{\alpha}{\beta}\right)\frac{\mathrm{d}\dot{\mathbf{u}}_n}{\mathrm{d}\theta}-(\Delta t)\left(1-\frac{\alpha}{2\beta}\right)\frac{\mathrm{d}\ddot{\mathbf{u}}_n}{\mathrm{d}\theta}\right].\end{aligned} \tag{44}$$

In Eq. (43), $(\mathbf{K}_{\mathrm{T}}^{\mathrm{stat}})_{n+1}$ denotes the consistent (or algorithmic) tangent (static) stiffness matrix of the structure/system, which is defined as the assembly of the element consistent tangent stiffness matrices as

$$(\mathbf{K}_{\mathrm{T}}^{\mathrm{stat}})_{n+1}=\frac{\partial\mathbf{R}(\mathbf{u}_{n+1})}{\partial\mathbf{u}_{n+1}}=\mathop{\mathbf{A}}_{e=1}^{\mathrm{Nel}}\left\{\frac{\partial\mathbf{R}^{(e)}(\mathbf{u}_{n+1})}{\partial\mathbf{u}_{n+1}^{(e)}}\right\}=\mathop{\mathbf{A}}_{e=1}^{\mathrm{Nel}}\left\{\int_{\Omega^{(e)}}\mathbf{B}^{\mathrm{T}}\mathbf{D}_{n+1}\mathbf{B}\,\mathrm{d}\Omega^{(e)}\right\}, \tag{45}$$

where $\mathbf{B}$ is the strain–displacement transformation matrix, and $\mathbf{D}_{n+1}$ denotes the point-wise matrix of material consistent (or algorithmic) tangent moduli obtained through consistent linearization of the constitutive law integration scheme [5,33,36], i.e.,

$$\mathbf{D}_{n+1}=\frac{\partial\boldsymbol{\sigma}_{n+1}(\boldsymbol{\sigma}_n,\boldsymbol{\epsilon}_n,\boldsymbol{\epsilon}-\boldsymbol{\epsilon}_n,\ldots)}{\partial\boldsymbol{\epsilon}_{n+1}}. \tag{46}$$

The consistent tangent modulus for the presented multi-yield-surface J_2 plasticity material model is computed by differentiating the stress tensor with strain tensor, following the explicit corrective iteration process of the stress computation. This modulus is an unsymmetrical fourth-order tensor (i.e., it exhibits only minor symmetry, $k_{ijkl}=k_{jikl}=k_{ijlk}=k_{jilk}$, but $k_{ijkl}\neq k_{klij}$). The derivation and implementation of the consistent tangent modulus was documented elsewhere in [30,33].

The second term on the right-hand-side (RHS) of Eq. (43) represents the partial derivative of the internal resisting force vector, $\mathbf{R}(\mathbf{u}_{n+1})$, with respect to sensitivity parameter θ under the condition that the nodal displacement vector $\mathbf{u}_{n+1}$ remains fixed. It is computed through direct stiffness assembly of the element resisting force derivatives as

$$\left.\frac{\partial\mathbf{R}(\mathbf{u}_{n+1}(\theta),\theta)}{\partial\theta}\right|_{\mathbf{u}_{n+1}}=\mathop{\mathbf{A}}_{e=1}^{\mathrm{Nel}}\left\{\int_{\Omega^{(e)}}\mathbf{B}^{\mathrm{T}}\left.\frac{\partial\boldsymbol{\sigma}(\boldsymbol{\epsilon}_{n+1}(\theta),\theta)}{\partial\theta}\right|_{\boldsymbol{\epsilon}_{n+1}}\mathrm{d}\Omega^{(e)}\right\}. \tag{47}$$

In the following section, computation of the unconditional (i.e., $\mathbf{u}_{n+1}$ is not fixed) stress sensitivities to parameters of the multi-yield-surface material plasticity model is presented in detail. The conditional (i.e., $\mathbf{u}_{n+1}$ is fixed) stress sensitivities are obtained as a special case of the unconditional ones.

3.3. Stress sensitivity for multi-yield-surface J_2 material plasticity model

Without loss of generality, the material sensitivity parameters that are considered in this paper are: (1) the low-strain shear modulus G, (2) the bulk modulus B, and (3) the shear strength $\tau_{\max}$ (see Fig. 1).

3.3.1. Parameter sensitivity of initial configuration of multi-yield-surface plasticity model

In this section, the sensitivities of the parameters (see Eqs. (3)–(10)) defining the initial configuration of the material model to the sensitivity parameter θ are derived. Differentiating Eq. (3) with respect to θ yields

$$\frac{\mathrm{d}\gamma_r}{\mathrm{d}\theta}=\frac{1}{(G\gamma_{\max}-\tau_{\max})^2}\cdot\left[\gamma_{\max}\cdot\frac{\mathrm{d}\tau_{\max}}{\mathrm{d}\theta}\cdot(G\gamma_{\max}-\tau_{\max})-\gamma_{\max}\cdot\tau_{\max}\cdot\left(\frac{\mathrm{d}G}{\mathrm{d}\theta}\cdot\gamma_{\max}-\frac{\mathrm{d}\tau_{\max}}{\mathrm{d}\theta}\right)\right]. \tag{48}$$

For each yield surface $\{f_j=0\}$ $(1\leqslant j\leqslant \mathrm{NYS}-1)$, Eq. (5) is differentiated with respect to θ as

$$\frac{\mathrm{d}\tau_j}{\mathrm{d}\theta}=\frac{\mathrm{d}\tau_{\max}}{\mathrm{d}\theta}\cdot\frac{j}{\mathrm{NYS}}, \tag{49}$$

$$\frac{\mathrm{d}\gamma_j}{\mathrm{d}\theta}=\frac{1}{(G\gamma_r-\tau_j)^2}\left[\left(\frac{\mathrm{d}\tau_j}{\mathrm{d}\theta}\cdot\gamma_r+\tau_j\cdot\frac{\mathrm{d}\gamma_r}{\mathrm{d}\theta}\right)\cdot(G\gamma_r-\tau_j)-\tau_j\gamma_r\cdot\left(\frac{\mathrm{d}G}{\mathrm{d}\theta}\cdot\gamma_r+G\cdot\frac{\mathrm{d}\gamma_r}{\mathrm{d}\theta}-\frac{\mathrm{d}\tau_j}{\mathrm{d}\theta}\right)\right]. \tag{50}$$

Differentiating Eqs. (6)–(10) with respect to θ yields

$$\frac{\mathrm{d}(\Delta\gamma)_j}{\mathrm{d}\theta}=\frac{\mathrm{d}\gamma_{j+1}}{\mathrm{d}\theta}-\frac{\mathrm{d}\gamma_j}{\mathrm{d}\theta}, \tag{51}$$

$$\frac{\mathrm{d}(\Delta\tau)_j}{\mathrm{d}\theta}=\frac{\mathrm{d}\tau_{j+1}}{\mathrm{d}\theta}-\frac{\mathrm{d}\tau_j}{\mathrm{d}\theta}, \tag{52}$$

$$\frac{\mathrm{d}K^{(j)}}{\mathrm{d}\theta}=\frac{3}{\sqrt{2}}\frac{\mathrm{d}\tau_j}{\mathrm{d}\theta}, \tag{53}$$

$$\frac{\mathrm{d}H^{(j)}}{\mathrm{d}\theta}=\frac{2}{(\Delta\gamma)_j^2}\left[\frac{\mathrm{d}(\Delta\tau)_j}{\mathrm{d}\theta}\cdot(\Delta\gamma)_j-(\Delta\tau)_j\cdot\frac{\mathrm{d}(\Delta\gamma)_j}{\mathrm{d}\theta}\right], \tag{54}$$

$$\frac{\mathrm{d}H'^{(j)}}{\mathrm{d}\theta}=\frac{2}{(2G-H^{(j)})^2}\left\{\left[\frac{\mathrm{d}G}{\mathrm{d}\theta}H^{(j)}+G\frac{\mathrm{d}H^{(j)}}{\mathrm{d}\theta}\right]\times\left((2G-H^{(j)})-GH^{(j)}\left(2\frac{\mathrm{d}G}{\mathrm{d}\theta}-\frac{\mathrm{d}H^{(j)}}{\mathrm{d}\theta}\right)\right)\right\}. \tag{55}$$

The outermost yield surface (failure surface) is characterized by $H^{(\mathrm{NYS})}=H'^{(\mathrm{NYS})}=0$. from which it follows that $\frac{\mathrm{d}H^{(\mathrm{NYS})}}{\mathrm{d}\theta}=0$ and $\frac{\mathrm{d}H'^{(\mathrm{NYS})}}{\mathrm{d}\theta}=0$. Furthermore, for each yield surface, the sensitivity to θ of the initial back-stress $\boldsymbol{\alpha}^{(j)}=\mathbf{0}$ (initial center of the yield surface) is zero, i.e., $\frac{\mathrm{d}\boldsymbol{\alpha}^{(j)}}{\mathrm{d}\theta}=\mathbf{0}$ $(1\leqslant j\leqslant \mathrm{NYS})$.

3.3.2. Stress response sensitivity

At each time or load step, once convergence is achieved for the response computation (at the structure level), the RHS of the response sensitivity equation (at the structure level), Eq. (43), is formed which includes the computation of the term $\left.\frac{\partial\mathbf{R}(\mathbf{u}_{n+1}(\theta),\theta)}{\partial\theta}\right|_{\mathbf{u}_{n+1}}$. The latter requires computation of the conditional (i.e., $\mathbf{u}_{n+1}$ is fixed case sensitives, $\left.\frac{\partial\boldsymbol{\sigma}(\boldsymbol{\epsilon}_{n+1}(\theta),\theta)}{\partial\theta}\right|_{\boldsymbol{\epsilon}_{n+1}}$, at each integration (Gauss) point. Eq. (43) is solved for the displacement response sensitivity $\frac{\mathrm{d}\mathbf{u}_{n+1}}{\mathrm{d}\theta}$. From the relationship between nodal displacements and strains at the element level, the strain and deviatoric strain response sensitivities ($\frac{\mathrm{d}\boldsymbol{\epsilon}_{n+1}}{\mathrm{d}\theta}$ and $\frac{\mathrm{d}\mathbf{e}_{n+1}}{\mathrm{d}\theta}$, respectively) can be readily obtained. Then, the unconditional (i.e., $\mathbf{u}_{n+1}$ is not fixed) stress response sensitivities at each integration (Gauss) point are computed as they are needed to form the RHS of the structural response sensitivity equation at the next time step. The conditional (i.e., $\mathbf{u}_{n+1}$ is fixed) stress response sensitivities are evaluated using the same equations as the unconditional ones, but imposing the constraint that $\mathbf{u}_{n+1}$ is fixed, which implies that the strain $\boldsymbol{\epsilon}_{n+1}$ is fixed for displacement-based finite elements.

Next, the stress response sensitivity to material constitutive parameters (G, B, and $\tau_{\max}$) is derived through consistent differentiation of the algorithm for stress response computation presented in Section 2. From Eq. (14), it follows that

$$\frac{\mathrm{d}\boldsymbol{\tau}^{\mathrm{tr}}_{n+1,0}}{\mathrm{d}\theta}=\frac{\mathrm{d}\boldsymbol{\tau}_{\mathrm{n}}}{\mathrm{d}\theta}+2\frac{\mathrm{d}G}{\mathrm{d}\theta}\Delta\mathbf{e}_{n+1}+2G\frac{\mathrm{d}\Delta\mathbf{e}_{n+1}}{\mathrm{d}\theta} \tag{56}$$

where $\Delta\mathbf{e}_{n+1}=\mathbf{e}_{n+1}-\mathbf{e}_n$ and thus $\frac{\mathrm{d}\Delta\mathbf{e}_{n+1}}{\mathrm{d}\theta}=\frac{\mathrm{d}\mathbf{e}_{n+1}}{\mathrm{d}\theta}-\frac{\mathrm{d}\mathbf{e}_n}{\mathrm{d}\theta}$. When computing the conditional stress sensitivity (see Eq. (47)) for which the strain $\boldsymbol{\epsilon}_{n+1}$ and therefore the deviatoric strain $\mathbf{e}_{n+1}$ remain fixed, $\frac{\mathrm{d}\mathbf{e}_{n+1}}{\mathrm{d}\theta}=\mathbf{0}$ and $\frac{\mathrm{d}\Delta\mathbf{e}_{n+1}}{\mathrm{d}\theta}=-\frac{\mathrm{d}\mathbf{e}_n}{\mathrm{d}\theta}$. This represents the only difference between conditional and unconditional stress response sensitivity computations. All the formulas for unconditional sensitivity computations derived in the sequel of Section 3.3 apply equally to conditional stress sensitivity computation.

The sensitivity of the contact stress $\boldsymbol{\tau}^*_{n+1,i}$ to parameter θ is obtained by differentiating Eq. (16) with respect to θ as

$$\frac{\mathrm{d}\boldsymbol{\tau}^*_{n+1,i}}{\mathrm{d}\theta}=\frac{1}{K^2_{n+1,i}}\left\{\left[\frac{\mathrm{d}K^{(m)}}{\mathrm{d}\theta}(\boldsymbol{\tau}^{\mathrm{tr}}_{n+1,i-1}-\boldsymbol{\alpha}^{(m)}_n)+K^{(m)}\left(\frac{\mathrm{d}\boldsymbol{\tau}^{\mathrm{tr}}_{n+1,i-1}}{\mathrm{d}\theta}-\frac{\mathrm{d}\boldsymbol{\alpha}^{(m)}_n}{\mathrm{d}\theta}\right)\right]\times K_{n+1,i}-K^{(m)}(\boldsymbol{\tau}^{\mathrm{tr}}_{n+1,i-1}-\boldsymbol{\alpha}^{(m)}_n)\frac{\mathrm{d}K_{n+1,i}}{\mathrm{d}\theta}\right\}+\frac{\mathrm{d}\boldsymbol{\alpha}^{(m)}_n}{\mathrm{d}\theta}, \tag{57}$$

where the sensitivity of $K_{n+1,\,i}$ to θ is obtained from Eq. (17) as

$$\frac{\mathrm{d}K_{n+1,i}}{\mathrm{d}\theta}=\frac{3}{2K_{n+1,i}}\left(\frac{\mathrm{d}\boldsymbol{\tau}^{\mathrm{tr}}_{n+1,i-1}}{\mathrm{d}\theta}-\frac{\mathrm{d}\boldsymbol{\alpha}^{(m)}_n}{\mathrm{d}\theta}\right):(\boldsymbol{\tau}^{\mathrm{tr}}_{n+1,i-1}-\boldsymbol{\alpha}^{(m)}_n). \tag{58}$$

Eq. (18) yields the following sensitivity to θ of the unit tensor normal to the yield surface at $\boldsymbol{\tau}^*_{n+1,i}$:

$$\frac{\mathrm{d}\mathbf{Q}_{n+1,i}}{\mathrm{d}\theta}=\frac{\left(\frac{\mathrm{d}\boldsymbol{\tau}^*_{n+1,i}}{\mathrm{d}\theta}-\frac{\mathrm{d}\boldsymbol{\alpha}^{(m)}_n}{\mathrm{d}\theta}\right)}{[(\boldsymbol{\tau}^*_{n+1,i}-\boldsymbol{\alpha}^{(m)}_n):(\boldsymbol{\tau}^*_{n+1,i}-\boldsymbol{\alpha}^{(m)}_n)]^{1/2}}-\frac{\left(\frac{\mathrm{d}\boldsymbol{\tau}^*_{n+1,i}}{\mathrm{d}\theta}-\frac{\mathrm{d}\boldsymbol{\alpha}^{(m)}_n}{\mathrm{d}\theta}\right):(\boldsymbol{\tau}^*_{n+1,i}-\boldsymbol{\alpha}^{(m)}_n)}{((\boldsymbol{\tau}^*_{n+1,i}-\boldsymbol{\alpha}^{(m)}_n):(\boldsymbol{\tau}^*_{n+1,i}-\boldsymbol{\alpha}^{(m)}_n))^{3/2}}\cdot(\boldsymbol{\tau}^*_{n+1,i}-\boldsymbol{\alpha}^{(m)}_n). \tag{59}$$

Then, the sensitivity of the plastic stress correction tensor is derived from Eq. (19) as

$$\begin{aligned}\frac{\mathrm{d}\mathbf{P}_{n+1,1}}{\mathrm{d}\theta}=&2\frac{\mathrm{d}G}{\mathrm{d}\theta}\frac{\mathbf{Q}_{n+1,1}:(\boldsymbol{\tau}^{\mathrm{tr}}_{n+1,0}-\boldsymbol{\tau}^*_{n+1,1})}{(H'^{(m)}+2G)}\mathbf{Q}_{n+1,1}\\&+2G\frac{\mathbf{Q}_{n+1,1}:(\boldsymbol{\tau}^{\mathrm{tr}}_{n+1,0}-\boldsymbol{\tau}^*_{n+1,1})}{(H'^{(m)}+2G)}\cdot\frac{\mathrm{d}\mathbf{Q}_{n+1,1}}{\mathrm{d}\theta}\\&+\frac{2G}{(H'^{(m)}+2G)^2}\left\{\left[\frac{\mathrm{d}\mathbf{Q}_{n+1,1}}{\mathrm{d}\theta}:(\boldsymbol{\tau}^{\mathrm{tr}}_{n+1,0}-\boldsymbol{\tau}^*_{n+1,1})\right.\right.\\&\left.+\mathbf{Q}_{n+1,1}:\left(\frac{\mathrm{d}\boldsymbol{\tau}^{\mathrm{tr}}_{n+1,0}}{\mathrm{d}\theta}-\frac{\mathrm{d}\boldsymbol{\tau}^*_{n+1,1}}{\mathrm{d}\theta}\right)\right](H'^{(m)}+2G)\\&\left.-\mathbf{Q}_{n+1,1}:(\boldsymbol{\tau}^{\mathrm{tr}}_{n+1,0}-\boldsymbol{\tau}^*_{n+1,1})\cdot\left(\frac{\mathrm{d}H'^{(m)}}{\mathrm{d}\theta}+2\frac{\mathrm{d}G}{\mathrm{d}\theta}\right)\right\}\mathbf{Q}_{n+1,1}\end{aligned} \tag{60}$$

for the first corrective iteration (subscript $i=1$) and from Eq. (20) as

$$\begin{aligned}\frac{\mathrm{d}\mathbf{P}_{n+1,i}}{\mathrm{d}\theta}=&\left[2\frac{\mathrm{d}G}{\mathrm{d}\theta}\frac{\mathbf{Q}_{n+1,i}:(\boldsymbol{\tau}^{\mathrm{tr}}_{n+1,i-1}-\boldsymbol{\tau}^*_{n+1,i})}{(H'^{(m)}+2G)}\mathbf{Q}_{n+1,i}\right.\\&\left.+2G\frac{\mathbf{Q}_{n+1,i}:(\boldsymbol{\tau}^{\mathrm{tr}}_{n+1,i-1}-\boldsymbol{\tau}^*_{n+1,i})}{(H'^{(m)}+2G)}\frac{\mathrm{d}\mathbf{Q}_{n+1,i}}{\mathrm{d}\theta}\right]\frac{(H'^{(m-1)}-H'^{(m)})}{H'^{(m-1)}}\\&+\frac{2G(H'^{(m-1)}-H'^{(m)})}{(H'^{(m)}+2G)^2\cdot H'^{(m-1)}}\left\{\left[\frac{\mathrm{d}\mathbf{Q}_{n+1,i}}{\mathrm{d}\theta}:(\boldsymbol{\tau}^{\mathrm{tr}}_{n+1,i-1}-\boldsymbol{\tau}^*_{n+1,i})\right.\right.\\&\left.+\mathbf{Q}_{n+1,i}:\left(\frac{\mathrm{d}\boldsymbol{\tau}^{\mathrm{tr}}_{n+1,i-1}}{\mathrm{d}\theta}-\frac{\mathrm{d}\boldsymbol{\tau}^*_{n+1,i}}{\mathrm{d}\theta}\right)\right](H'^{(m)}+2G)\\&\left.-\mathbf{Q}_{n+1,i}:(\boldsymbol{\tau}^{\mathrm{tr}}_{n+1,i-1}-\boldsymbol{\tau}^*_{n+1,i})\left(\frac{\mathrm{d}H'^{(m)}}{\mathrm{d}\theta}+2\frac{\mathrm{d}G}{\mathrm{d}\theta}\right)\right\}\mathbf{Q}_{n+1,i}\\&+2G\frac{\mathbf{Q}_{n+1,i}:(\boldsymbol{\tau}^{\mathrm{tr}}_{n+1,i-1}-\boldsymbol{\tau}^*_{n+1,i})}{(H'^{(m)}+2G)}\\&\cdot\left[\frac{\mathrm{H}'^{(m)}}{[H'^{(m-1)}]^2}\frac{\mathrm{d}H'^{(m-1)}}{\mathrm{d}\theta}-\frac{1}{H'^{(m-1)}}\frac{\mathrm{d}H'^{(m)}}{\mathrm{d}\theta}\right]\mathbf{Q}_{n+1,i}\end{aligned} \tag{61}$$

for the second and subsequent corrective iterations ($i = 2, 3, 4, \ldots$). The sensitivity to θ of the trial stress tensor after the ith plastic correction is obtained from Eq. (21) as

$$\frac{\mathrm{d}\boldsymbol{\tau}^{\mathrm{tr}}_{n+1,i}}{\mathrm{d}\theta} = \frac{\mathrm{d}\boldsymbol{\tau}^{\mathrm{tr}}_{n+1,i-1}}{\mathrm{d}\theta} + \frac{\mathrm{d}\mathbf{P}_{n+1,i}}{\mathrm{d}\theta} \quad (i = 1, 2, \ldots). \tag{62}$$

If the trial stress $\boldsymbol{\tau}^{\mathrm{tr}}_{n+1,i}$ lies outside the next outer yield surface $\{f_{m+1} = 0\}$, the active yield surface index is set to $m = m + 1$, the corrective iteration number is set to $i = i + 1$, the plastic correction process and its sensitivity (Eqs. (57)–(62)) is repeated until the trial stress falls inside the next outer yield surface.

After "convergence" of the deviatoric stress $\boldsymbol{\tau}^{\mathrm{tr}}_{n+1,i}$ is achieved, the sensitivity to θ of the updated volumetric stress $\sigma^{\mathrm{vol}}_{n+1}$ is computed from Eq. (22) as

$$\frac{\mathrm{d}\sigma^{\mathrm{vol}}_{n+1}}{\mathrm{d}\theta} = \frac{\mathrm{d}\sigma^{\mathrm{vol}}_{n}}{\mathrm{d}\theta} + \frac{\mathrm{d}B}{\mathrm{d}\theta}\cdot(\Delta\epsilon_{n+1})_{\mathrm{ii}} + B\cdot\frac{\mathrm{d}(\Delta\epsilon_{n+1})_{\mathrm{ii}}}{\mathrm{d}\theta}, \tag{63}$$

where $\frac{\mathrm{d}(\Delta\epsilon_{n+1})_{\mathrm{ii}}}{\mathrm{d}\theta} = \frac{\mathrm{d}\Delta\epsilon_{n+1,11}}{\mathrm{d}\theta} + \frac{\mathrm{d}\Delta\epsilon_{n+1,22}}{\mathrm{d}\theta} + \frac{\mathrm{d}\Delta\epsilon_{n+1,33}}{\mathrm{d}\theta}$. It is worth noting that in the process of computing the conditional stress sensitivities, the quantity $\frac{\mathrm{d}(\Delta\epsilon_{n+1})_{\mathrm{ii}}}{\mathrm{d}\theta} = 0$, since $\mathbf{u}_{n+1}$ is considered fixed. Finally, the sensitivity to θ of the total stress is obtained from Eq. (23) as

$$\frac{\mathrm{d}\boldsymbol{\sigma}_{n+1}}{\mathrm{d}\theta} = \frac{\mathrm{d}\boldsymbol{\tau}_{n+1}}{d\theta} + \frac{\mathrm{d}\sigma^{\mathrm{vol}}_{n+1}}{\mathrm{d}\theta}\cdot\mathbf{I}. \tag{64}$$

After the sensitivity to θ of the current stress $\boldsymbol{\sigma}_{n+1}$ is computed, the sensitivity of the hardening parameters, namely the back-stress (center of the yield surface) ($1 \leqslant i \leqslant m$) for the current active and each of the inner yield surfaces ($\boldsymbol{\alpha}^{(i)}_n, 1 \leqslant i \leqslant m$), must be computed and updated (in the case of unconditional stress sensitivity only), which is the object of the next section. The sensitivities of the hardening parameters are needed for computing the conditional and unconditional stress sensitivities at the next time step (i.e., at t_{n+2}).

3.3.3. Sensitivity of hardening parameters of active and inner yield surfaces

In this section, the sensitivity to θ of the kinematic hardening parameters of the active and inner yield surfaces are derived by differentiating with respect to θ the updating equations for these hardening parameters presented in Section 2.3 (Eqs. (24)–(38)).

From Eq. (25), it follows that the sensitivity to θ of the deviatoric stress tensor $\boldsymbol{\tau}_{\mathrm{T}}$ at point T of the m-th yield surface (see Fig. 3), is given by

$$\frac{\mathrm{d}\boldsymbol{\tau}_{\mathrm{T}}}{\mathrm{d}\theta} = \frac{\mathrm{d}\boldsymbol{\alpha}^{(m)}_n}{\mathrm{d}\theta} + \frac{\mathrm{d}\xi}{\mathrm{d}\theta}(\boldsymbol{\tau}_{n+1} - \boldsymbol{\alpha}^{(m)}_n) + \xi\left(\frac{\mathrm{d}\boldsymbol{\tau}_{n+1}}{\mathrm{d}\theta} - \frac{\mathrm{d}\boldsymbol{\alpha}^{(m)}_n}{\mathrm{d}\theta}\right), \tag{65}$$

where $\frac{\mathrm{d}\xi}{\mathrm{d}\theta}$ is obtained from Eq. (27) as

$$\frac{\mathrm{d}\xi}{\mathrm{d}\theta} = \frac{-\frac{\mathrm{d}A}{\mathrm{d}\theta}\xi^2 - \frac{\mathrm{d}B}{\mathrm{d}\theta}\xi - \frac{\mathrm{d}C}{\mathrm{d}\theta}}{2A\xi + B} \tag{66}$$

and where $\frac{\mathrm{d}A}{\mathrm{d}\theta}$, $\frac{\mathrm{d}B}{\mathrm{d}\theta}$, and $\frac{\mathrm{d}C}{\mathrm{d}\theta}$ are obtained in turn from Eqs. (28)–(30) as

$$\frac{\mathrm{d}A}{\mathrm{d}\theta} = 2\left(\frac{\mathrm{d}\boldsymbol{\tau}_{n+1}}{\mathrm{d}\theta} - \frac{\mathrm{d}\boldsymbol{\alpha}^{(m)}_n}{\mathrm{d}\theta}\right) : (\boldsymbol{\tau}_{n+1} - \boldsymbol{\alpha}^{(m)}_n), \tag{67}$$

$$\frac{\mathrm{d}B}{\mathrm{d}\theta} = 2\left(\frac{\mathrm{d}\boldsymbol{\alpha}^{(m)}_n}{\mathrm{d}\theta} - \frac{\mathrm{d}\boldsymbol{\alpha}^{(m+1)}_n}{\mathrm{d}\theta}\right) : (\boldsymbol{\tau}_{n+1} - \boldsymbol{\alpha}^{(m)}_n) + 2(\boldsymbol{\alpha}^{(m)}_n - \boldsymbol{\alpha}^{(m+1)}_n) : \left(\frac{\mathrm{d}\boldsymbol{\tau}_{n+1}}{\mathrm{d}\theta} - \frac{\mathrm{d}\boldsymbol{\alpha}^{(m)}_n}{\mathrm{d}\theta}\right), \tag{68}$$

$$\frac{\mathrm{d}C}{\mathrm{d}\theta} = 2\left(\frac{\mathrm{d}\boldsymbol{\alpha}^{(m)}_n}{\mathrm{d}\theta} - \frac{\mathrm{d}\boldsymbol{\alpha}^{(m+1)}_n}{\mathrm{d}\theta}\right) : (\boldsymbol{\alpha}^{(m)}_n - \boldsymbol{\alpha}^{(m+1)}_n) - \frac{4}{3}K^{(m+1)}\cdot\frac{\mathrm{d}K^{(m+1)}}{\mathrm{d}\theta}. \tag{69}$$

Then, the sensitivity to θ of the translation direction $\boldsymbol{\mu}_{n+1}$ is computed by differentiating Eq. (24) with respect to θ as

$$\frac{\mathrm{d}\boldsymbol{\mu}_{n+1}}{\mathrm{d}\theta} = \left[\frac{\mathrm{d}\boldsymbol{\tau}_{\mathrm{T}}}{\mathrm{d}\theta} - \frac{\mathrm{d}\boldsymbol{\alpha}^{(m)}_n}{\mathrm{d}\theta}\right] - \left(\frac{\frac{\mathrm{d}K^{(m)}}{\mathrm{d}\theta}K^{(m+1)} - K^{(m)}\frac{\mathrm{d}K^{(m+1)}}{\mathrm{d}\theta}}{[K^{(m+1)}]^2}\right)[\boldsymbol{\tau}_{\mathrm{T}} - \boldsymbol{\alpha}^{(m+1)}_n] - \frac{K^{(m)}}{K^{(m+1)}}\left[\frac{\mathrm{d}\boldsymbol{\tau}_{\mathrm{T}}}{\mathrm{d}\theta} - \frac{\mathrm{d}\boldsymbol{\alpha}^{(m+1)}_n}{\mathrm{d}\theta}\right]. \tag{70}$$

After $\frac{\mathrm{d}\boldsymbol{\mu}_{n+1}}{\mathrm{d}\theta}$ is obtained, the sensitivity to θ of the translation parameter ζ is derived from Eq. (32) as

$$\frac{\mathrm{d}\zeta}{\mathrm{d}\theta} = \frac{-\frac{\mathrm{d}A'}{\mathrm{d}\theta}\zeta^2 - \frac{\mathrm{d}B'}{\mathrm{d}\theta}\zeta - \frac{\mathrm{d}C'}{\mathrm{d}\theta}}{2A'\zeta + B'}, \tag{71}$$

where $\frac{\mathrm{d}A'}{\mathrm{d}\theta}$, $\frac{\mathrm{d}B'}{\mathrm{d}\theta}$, and $\frac{\mathrm{d}C'}{\mathrm{d}\theta}$ are obtained from Eqs. (33)–(35) as

$$\frac{\mathrm{d}A'}{\mathrm{d}\theta} = 2\frac{\mathrm{d}\boldsymbol{\mu}_{n+1}}{\mathrm{d}\theta} : \boldsymbol{\mu}_{n+1}, \tag{72}$$

$$\frac{\mathrm{d}B'}{\mathrm{d}\theta} = -2\frac{\mathrm{d}\boldsymbol{\mu}_{n+1}}{\mathrm{d}\theta} : (\boldsymbol{\tau}_{n+1} - \boldsymbol{\alpha}^{(m)}_n) - 2\boldsymbol{\mu}_{n+1} : \left(\frac{\mathrm{d}\boldsymbol{\tau}_{n+1}}{\mathrm{d}\theta} - \frac{\mathrm{d}\boldsymbol{\alpha}^{(m)}_n}{\mathrm{d}\theta}\right), \tag{73}$$

$$\frac{\mathrm{d}C'}{\mathrm{d}\theta} = 2\left(\frac{\mathrm{d}\boldsymbol{\tau}_{n+1}}{\mathrm{d}\theta} - \frac{\mathrm{d}\boldsymbol{\alpha}^{(m)}_n}{\mathrm{d}\theta}\right) : (\boldsymbol{\tau}_{n+1} - \boldsymbol{\alpha}^{(m)}_n) - \frac{4}{3}K^{(m)}\cdot\frac{\mathrm{d}K^{(m)}}{\mathrm{d}\theta}. \tag{74}$$

Finally, from Eq. (36) the sensitivity to θ of the updated back-stress (center of yield surface) of the current active yield surface is given by

$$\frac{\mathrm{d}\boldsymbol{\alpha}^{(m)}_{n+1}}{\mathrm{d}\theta} = \frac{\mathrm{d}\boldsymbol{\alpha}^{(m)}_n}{\mathrm{d}\theta} + \frac{\mathrm{d}\zeta}{\mathrm{d}\theta}\boldsymbol{\mu}_{n+1} + \zeta\frac{\mathrm{d}\boldsymbol{\mu}_{n+1}}{\mathrm{d}\theta}. \tag{75}$$

The sensitivity to θ of the updated back-stress of each of the inner yield surfaces are obtained from Eq. (38) as

$$\frac{\mathrm{d}\boldsymbol{\alpha}^{(i)}_{n+1}}{\mathrm{d}\theta} = \frac{\mathrm{d}\tau_{n+1}}{\mathrm{d}\theta} - \frac{K^{(m)}\frac{\mathrm{d}K^{(i)}}{\mathrm{d}\theta}(\boldsymbol{\tau}_{n+1} - \boldsymbol{\alpha}^{(m)}_{n+1}) + K^{(m)}K^{(i)}\left(\frac{\mathrm{d}\tau_{n+1}}{\mathrm{d}\theta} - \frac{\mathrm{d}\boldsymbol{\alpha}^{(m)}_{n+1}}{\mathrm{d}\theta}\right) - \frac{\mathrm{d}K^{(m)}}{\mathrm{d}\theta}K^{(i)}(\boldsymbol{\tau}_{n+1} - \boldsymbol{\alpha}^{(m)}_{n+1})}{(K^{(m)})^2}, \tag{76}$$

where $1 \leqslant i \leqslant m - 1$.

4. Application examples

4.1. Three-dimensional block of clay subjected to quasi-static cyclic loading

In this section, a three-dimensional (3D) solid block of dimensions 1 m × 1 m × 1 m subjected to quasi-static cyclic loading in both horizontal directions simultaneously, see Fig. 5, is used as first application and validation example. The block is discretized into 8 brick elements defined as displacement-based eight-noded, trilinear isoparametric finite elements with eight integration points each. The block material consists of a medium clay with the following material constitutive parameters [19]: low-strain shear modulus $G = 6.0 \times 10^4$ kPa, elastic bulk modulus $B = 2.4 \times 10^5$ kPa, ($\Rightarrow$ Poisson's ratio = 0.38), and maximum shear stress $\tau_{\max} = 30$ kPa. The bottom nodes of the finite element (FE) model are fixed and top nodes $\{A, B, C\}$ and $\{A, D, E\}$ are subjected to five cycles of harmonic, 90 degrees out-of-phase, concentrated horizontal forces $F_{x_1}(t) = 2.0\sin(0.2\pi t)$[kN] and $F_{x_2}(t) = 2.0\sin(0.2\pi t + 0.5\pi)$[kN], respectively. The number of yield surfaces is set to 20. A time increment of $\Delta t = 0.01$ s is used to integrate the equations of quasi-static equilibrium (i.e., without inertia and damping effects).

The displacement response of node A (see Fig. 5) in the x_1-direction is shown in Fig. 6 as a function of the force $F_{x_1}(t)$, while the hysteretic shear stress–strain response ($\sigma_{31} - \varepsilon_{31}$) at Gauss point G (see Fig. 5) is plotted in Fig. 7. These figures indicate that significant yielding of the clay is observed during the cyclic loading considered.

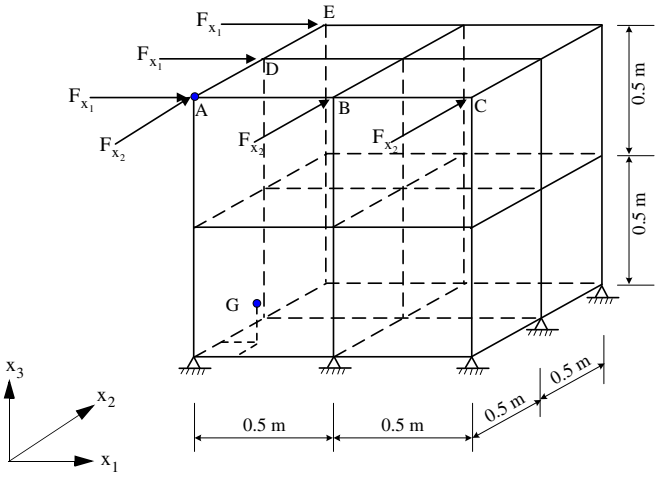

Fig. 5. Solid block of clay subjected to horizontal quasi-static cyclic loading under undrained condition.

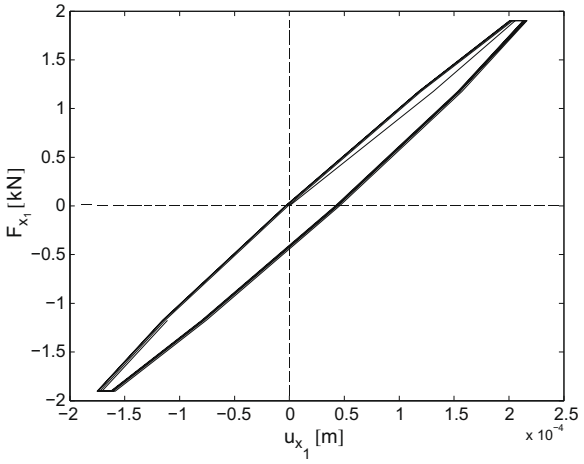

Fig. 6. Force–displacement response at node *A*.

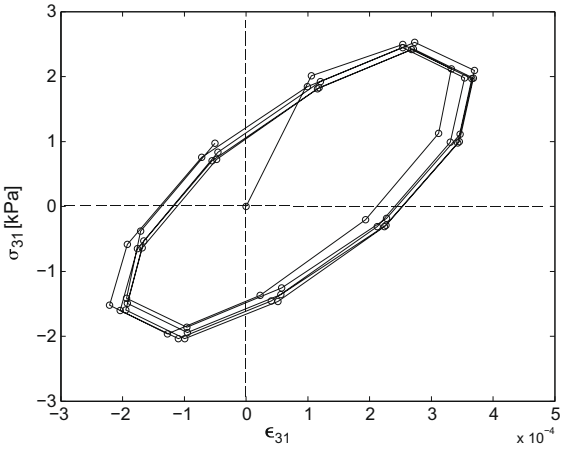

Fig. 7. Shear stress–strain response at Gauss point *G* (see Fig. 5).

The sensitivities of the displacement response $u(t)$ of node *A* in the x_1-direction to the shear modulus *G*, bulk modulus *B* and shear strength τ_{max} computed using the DDM are compared in Figs. 8, 10

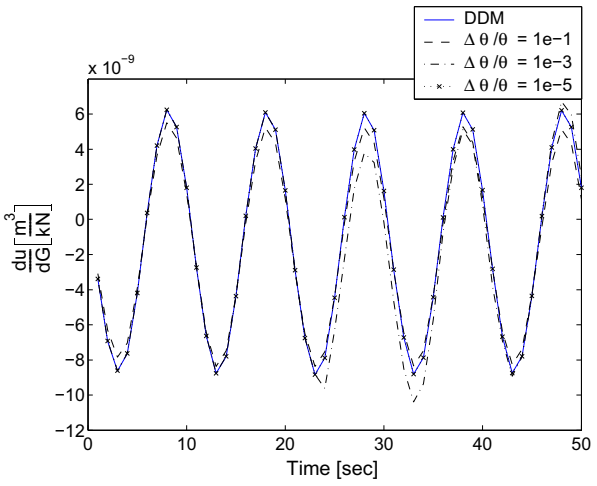

Fig. 8. Sensitivity of displacement response $u(t)$ of node *A* in the x_1-direction to the low-strain shear modulus *G* computed using DDM and forward finite difference for three different values of relative parameter perturbation $\Delta\theta/\theta$.

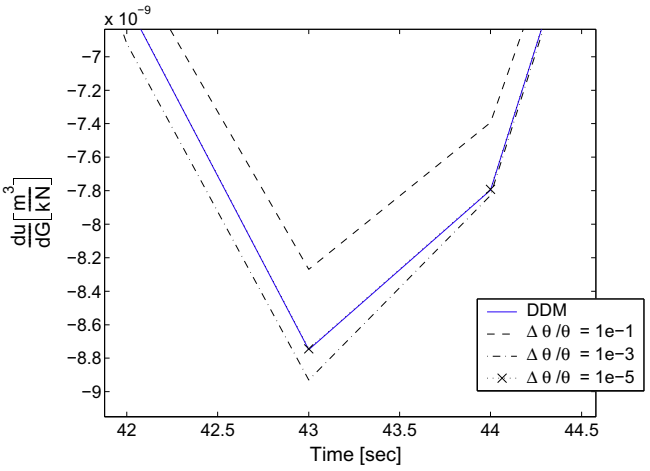

Fig. 9. Sensitivity of displacement response $u(t)$ of node *A* in the x_r direction to the low-strain shear modulus *G* computed using DDM and forward finite difference (zoom view of Fig. 8).

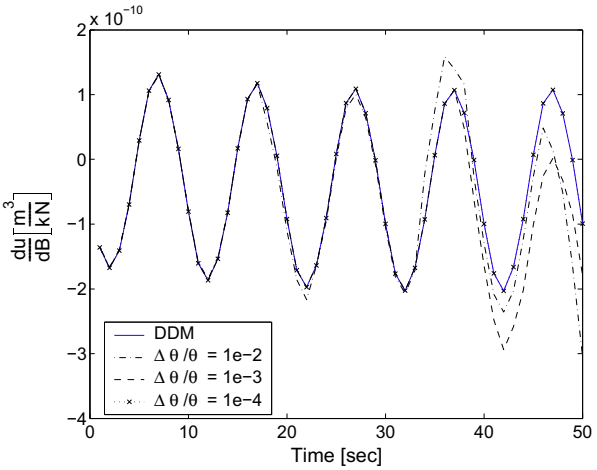

Fig. 10. Sensitivity of displacement response $u(t)$ of node *A* in the x_1-direction to the bulk modulus *B* computed using DDM and forward finite difference for three different values of relative parameter perturbation $\Delta\theta/\theta$.

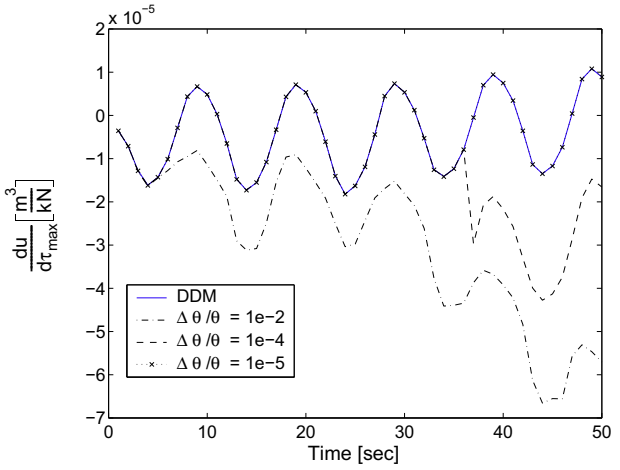

Fig. 11. Sensitivity of displacement response $u(t)$ of node A in the x_1-direction to the shear strength τ_{max} computed using DDM and FFD for three different values of relative parameter perturbation $\Delta\theta/\theta$.

and 11, respectively, with the corresponding sensitivities estimated using the forward finite difference (FFD) method with increasingly small perturbations $\Delta\theta$ of the sensitivity parameter θ. Fig. 9 shows a zoom view from Fig. 8 that allows to better appreciate the convergence trend of the FFD results to the DDM one. In all cases, it is observed that the FFD results converge asympotically to the DDM results as $\Delta\theta/\theta$ becomes increasingly small. In each case, particular attention was given to the choice of the lower value of the parameter perturbation so as to avoid numerical problems related to round-off errors. A perfect match between DDM and FFD results was achieved with relative perturbation $\Delta\theta/\theta$ of 1.0e−5, 1.0e−5 and 1.0e−4, respectively, for the shear modulus G, bulk modulus B, and shear strength τ_{max}.

4.2. Multi-layered soil column subjected to earthquake base excitation

The second benchmark problem consists of a multi-layered soil column subjected to earthquake base excitation. This soil column is representative of the local soil condition at the site of the Humboldt Bay Middle Channel Bridge near Eureka in northern California [16]. A Multi-yield-surface J_2 plasticity model with 20 yield surfaces and different parameter sets given in Table 1 is used to represent the various soil layers. The soil column is discretized into a 2D plane-strain finite element model consisting of 28 four-node quadratic bilinear isoparametric elements with four Gauss points each as shown in Fig. 12. The soil column is assumed to be under simple shear condition, and the corresponding nodes at the same depth on the left and right boundaries are tied together for both horizontal and vertical displacements. First, gravity is applied quasi-statically and then base excitation is applied dynamically. The total horizontal acceleration at the base of the soil column, see Fig. 13, was obtained from another study [16] through deconvolution of a ground surface free field motion. The Newmark-beta direct step-by-step integration method with parameters $\beta = 0.2756$ and $\gamma = 0.55$ is used with a constant time step $\Delta t = 0.01$ s for integrating the equations of motion of the soil column. The horizontal displacement response of the soil column (relative to the base) at the top of each soil layer is shown in Fig. 14. The shear stress–strain (σ_{xz},ε_{xz}) hysteretic response at Gauss points C, D, E, F (see Fig. 12) of the soil column is shown in Fig. 15. The response simulation results in Figs. 14 and 15 indicate that the soil material undergoes significant nonlinear behavior.

Table 1
Material properties of various layers of soil column (from ground surface to base of soil column).

Material #	G (kPa)	B (kPa)	τ_{max} (kPa)
1	54450	1.6×10^5	33
2	33800	1.0×10^5	26
3	96800	2.9×10^5	44
4	61250	1.8×10^5	35
5	180000	5.4×10^5	60
6	369800	1.1×10^6	86

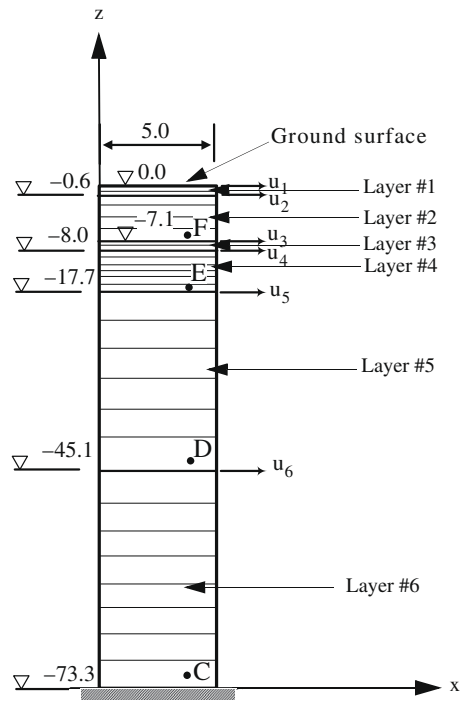

Fig. 12. Layered soil column subjected to total base acceleration with finite element mesh in thin lines (unit: [m]). Soil layers are numbered from top to bottom.

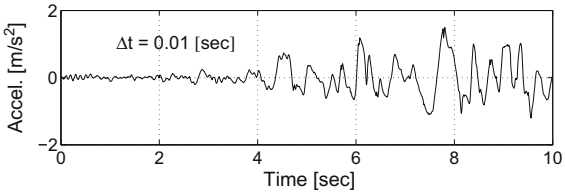

Fig. 13. Total acceleration time history at the base of the soil column.

Response sensitivity analysis is performed with the low-strain shear modulus G_i, the bulk modulus B_i, and the shear strength $\tau_{max,\,i}$ of the various soil layers (subscript i denotes the soil layer number, see Fig. 12) selected as sensitivity parameters. The DDM-based response sensitivity results are verified using the FFD method. Representative comparisons between response sensitivities obtained using DDM and FFD with increasingly smaller perturbations of the sensitivity parameters are shown in Figs. 16–21. From these figures and closeups, the FFD results are shown to converge asymptotically to the corresponding DDM results as the perturbation of the sensitivity parameter becomes increasingly small.

Finite element response sensitivity analysis can be used as a tool to investigate the relative importance of various system parameters in regards to the system response. Normalized

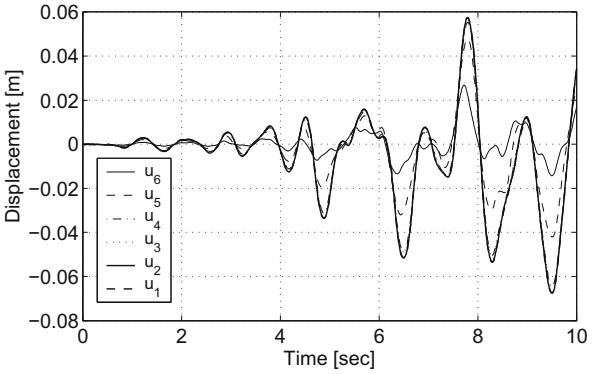

Fig. 14. Relative horizontal displacement time histories at the top of each layer of the soil column (see Fig. 12).

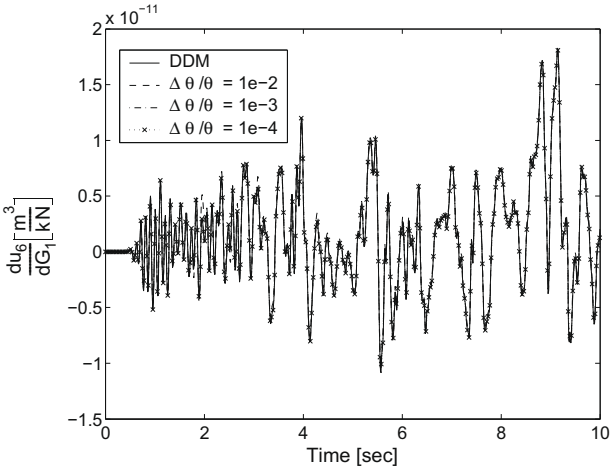

Fig. 16. Sensitivity of displacement response u_6 (see Fig. 12) to shear modulus G_1 obtained using DDM and FFD with increasingly small perturbations of sensitivity parameter.

response sensitivities (obtained through scaling each response sensitivity by the nominal value of the corresponding sensitivity parameter) can be used to quantify the relative importance of system parameters. Each normalized sensitivity can be interpreted as "100 times the change in the considered response quantity due to one percent change in the corresponding sensitivity parameter". As a first illustration, Fig. 22 shows the normalized sensitivities of the horizontal displacement response of the soil column top (ground surface) to the six most sensitive material parameters based on the peak (absolute) value of the normalized response sensitivity time history. These results indicate that the ground surface horizontal displacement response is most sensitive to, in order of decreasing importance: (1) $\tau_{\max,\,4}$, (2) $\tau_{\max,\,5}$, (3) $\tau_{\max,\,6}$, (4) G_4, (5) G_5, (6) G_6. Thus, the shear strength parameters of the bottom soil layers are very important in controlling the ground surface displacement response, since the soil undergoes significant nonlinearities when responding the earthquake excitation considered. This type of information may be extremely useful to geotechnical engineers seeking an optimum strategy (for example among various ground improvement techniques) to reduce the maximum ground surface displacement response during an earthquake. FE response sensitivities to material parameters are also invaluable to engineers when performing FE model updating, since they point to the most sensitive parameters which should be adjusted or

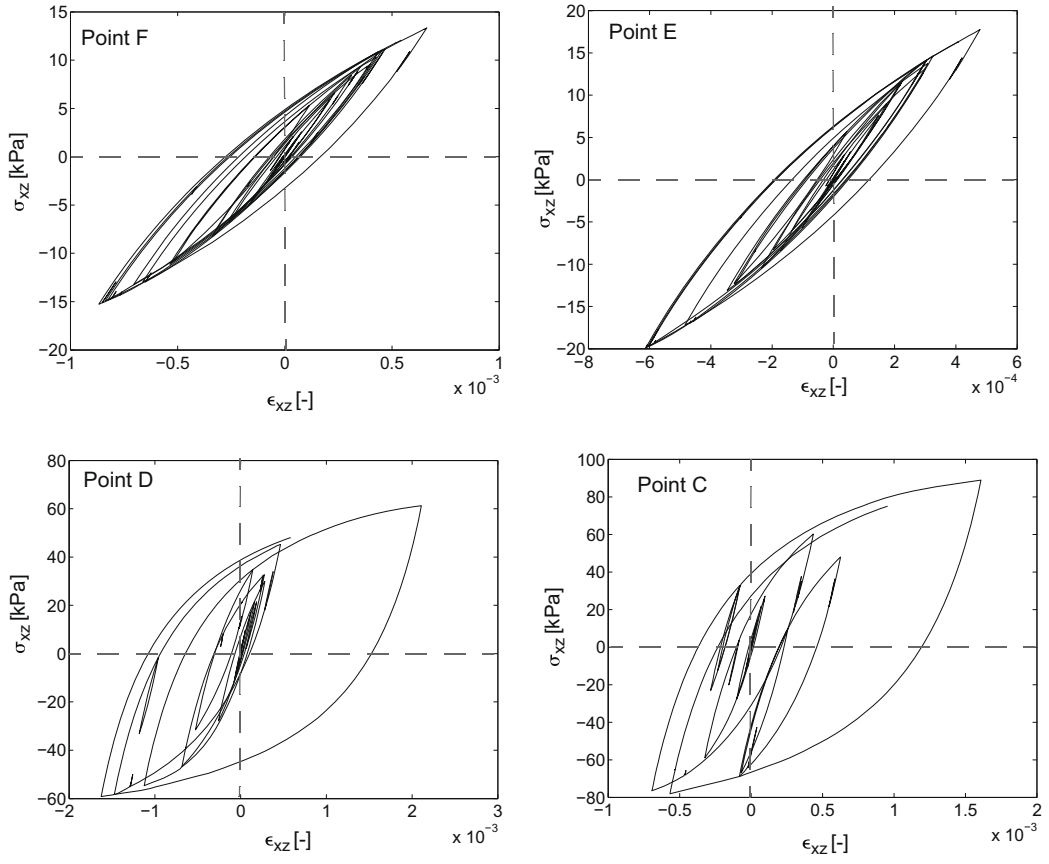

Fig. 15. Shear stress–strain hysteric responses at Gauss points C, D, E, and F (see Fig. 12).

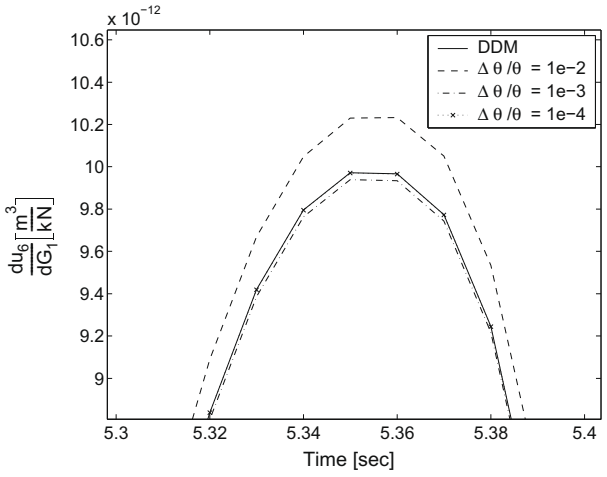

Fig. 17. Sensitivity of displacement response u_6 (see Fig. 12) to shear modulus G_1 obtained using DDM and FFD with increasingly small perturbations of sensitivity parameter (zoom view of Fig. 16).

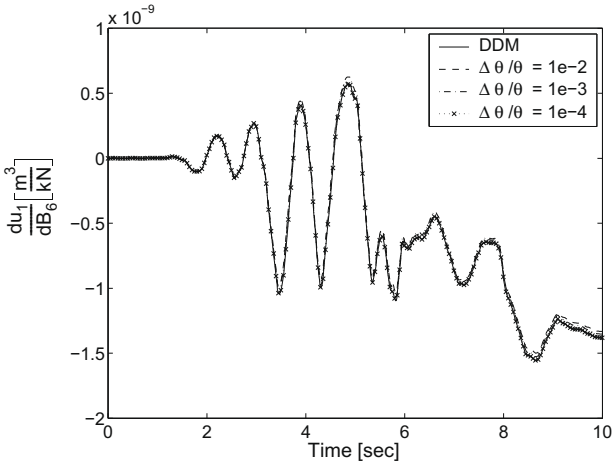

Fig. 18. Sensitivity of displacement response u_1 (see Fig. 12) to bulk modulus B_6 obtained using DDM and FFD with increasingly small perturbations of sensitivity parameter.

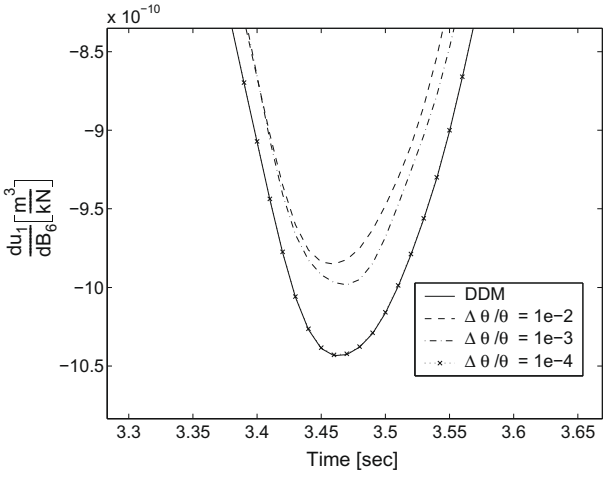

Fig. 19. Sensitivity of displacement response u_j (see Fig. 12) to bulk modulus B_6 obtained using DDM and FFD with increasingly small perturbations of sensitivity parameter (zoom view of Fig. 18).

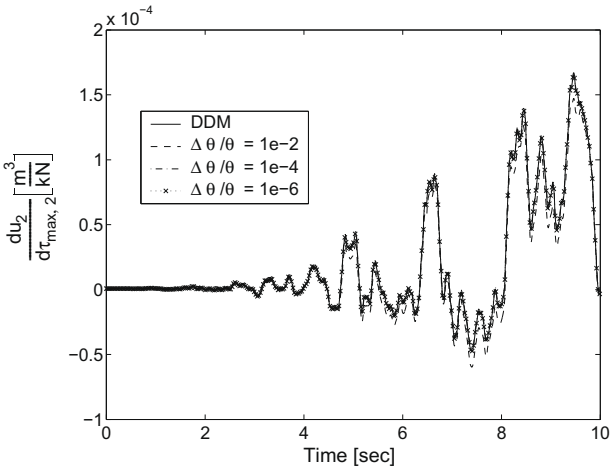

Fig. 20. Sensitivity of displacement response u_2 (see Fig. 12) to shear strength $\tau_{max,2}$ obtained using DDM and FFD with increasingly small perturbations of sensitivity parameter.

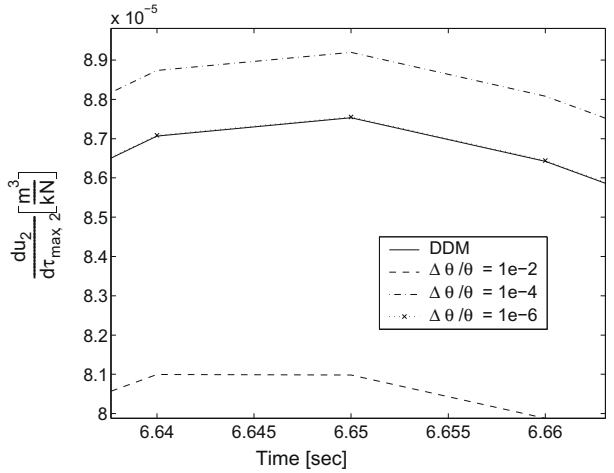

Fig. 21. Sensitivity of displacement response u_2 (see Fig. 12) to shear strength $\tau_{max,2}$ obtained using DDM and FFD with increasingly small perturbations of sensitivity parameter (zoom view of Fig. 20).

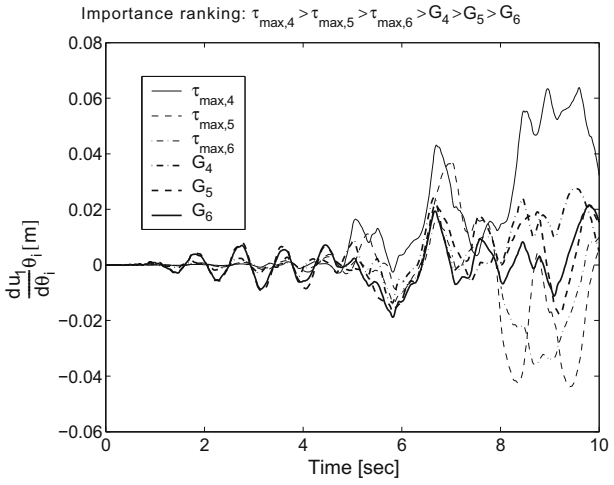

Fig. 22. Relative importance of material parameters on horizontal displacement response of ground surface (top of soil column, see Fig. 12).

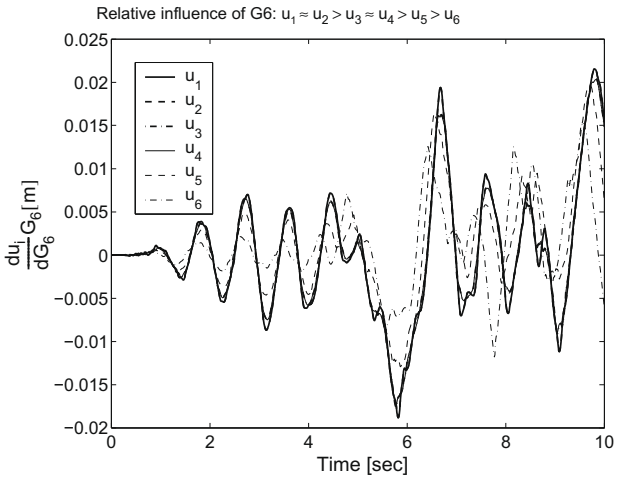

Fig. 23. Relative influence of shear modulus G_6 on horizontal displacement response of soil column at different soil layers (see Fig. 12).

calibrated with the highest priority. In a second illustration of the use of response sensitivity analysis, the effects of the low-strain shear modulus G_6 (of bottom soil layer) on the relative horizontal displacement response of the soil column at various soil layers are investigated. Fig. 23 shows the normalized sensitivities to G_6 of the horizontal displacement response of the soil column at various soil layers (u_1 through u_6). From these results, it follows that the ranking of the displacement responses u1 through u_6, in decreasing order of their sensitivity to G_6, is: (1) u_1 and u_2, (2) u_3 and u_4, (3) u_5, (4) u_6. These results indicate that the low-strain shear stiffness of the deepest soil layer affects most the soil response at the ground surface level.

For the two application examples presented above, convergence of the FFD response sensitivity results to the ones based on DDM validates the DDM-based algorithms for response sensitivity computation presented in this paper as well as their computer implementation. Regarding response sensitivity computation using the FFD, it is worth mentioning the "step-size dilemma" [7,37]: if the parameter perturbation $\Delta\theta$ is selected to be small, so as to reduce the truncation error, the condition error (due to round-off errors) may be excessive. In some cases, there may not be any value of the parameter perturbation $\Delta\theta$ which yields an acceptable error.

5. Conclusions

The direct differentiation method (DDM) is a general, accurate and efficient method to compute finite element (FE) response sensitivities to FE model parameters, especially in the case on nonlinear materials. This paper applies the DDM-based response sensitivity analysis methodology to a pressure independent multi-yield-surface J_2 plasticity material model, which has been used extensively to simulate the behavior of nonlinear clay soil material subjected to static and dynamic loading conditions. The algorithm developed is implemented in a software framework for finite element analysis of structural and/or geotechnical systems. Two application examples are presented to validate, using forward finite difference analysis, the response sensitivity results obtained from the proposed DDM-based algorithm. The second application example is also employed to illustrate the use of finite element response sensitivity analysis to investigate the relative importance of material parameters on system response.

The algorithm developed herein for nonlinear finite element response sensitivity analysis of geotechnical systems modeled using the multi-yield-surface J_2 plasticity model has direct applications in optimization, reliability analysis, and nonlinear FE model updating.

Acknowledgements

Support of this research by the Pacific Earthquake Engineering Research (PEER) Center through the Earthquake Engineering Research Centers Program of the National Science Foundation under Award No. EEC-9701568 and by Lawrence Livermore National Laboratory with Dr. David McCallen as Program Leader is gratefully acknowledged. Any opinions, findings, conclusions, or recommendations expressed in this publication are those of the authors and do not necessarily reflect the views of the sponsors.

References

[1] O. Ditlevsen, H.O. Madsen, Structural Reliability Methods, Wiley, 1996.
[2] M. Kleiber, T.D. Hien, H. Antunez, P. Kowalczyk, Parameter Sensitivity in Nonlinear Mechanics – Theory and Finite Element Computations, John Wiley & Sons, 1997.
[3] Y. Zhang, A. Der Kiureghian, Dynamic response sensitivity of inelastic structures, Comput. Methods Appl. Mech. Engrg. 108 (1993) 23–36.
[4] J.P. Conte, Finite element response sensitivity analysis in earthquake engineering, in: Spencer, Hu, Swets, Zeitlinger (Eds.), Earthquake Engineering Frontiers in the New Millennium, 2001, pp. 395–401.
[5] J.P. Conte, P.K. Vijalapura, M. Meghella, Consistent finite element response sensitivity analysis, J. Engrg. Mech., ASCE 129 (12) (2003) 1380–1393.
[6] J.P. Conte, M. Barbato, E. Spacone, Finite element response sensitivity analysis using force-based frame models, Int. J. Numer. Methods Engrg. 59 (13) (2004) 1781–1820.
[7] Q. Gu, J.P. Conte, Convergence studies in nonlinear finite element response sensitivity analysis, in: Ninth International Conference on Applications of Statistics and Probability in Civil Engineering, Berkeley, California, USA, July 2003.
[8] M.H. Scott, P. Franchin, G.L. Fenves, F.C. Filippou, Response sensitivity for nonlinear beam-column elements, J. Struct. Engrg. 130 (9) (2004) 281–1288.
[9] T. Haukaas, A. Der Kiureghian, Strategies for finding the design point in nonlinear finite element reliability analysis, J. Probabilist. Engrg. Mech. 21 (2) (2006) 133–147.
[10] W.D. Iwan, On a class of models for the yielding behavior of continuous and composite systems, J. Appl. Mech., Trans. ASCE 34 (E3) (1967) 612–617.
[11] A. Mroz, On the description of anisotropic workhardening, J. Mech. Phys. Solids, London 15 (1967) 163–175.
[12] J.H. Prevost, Mathematical modelling of monotonic and cyclic undrained clay behavior, Int. J. Numer. Anal. Methods Geomech. 1 (1977) 195–216.
[13] J.H. Prevost, Plasticity theory for soil stress–strain behavior, J. Engrg. Mech. Div. 104 (5) (1978) 1177–1194.
[14] J.H. Prevost, Anistropic undrained stress–strain behavior of clays, J. Geotech. Engrg. Div., ASCE 104 (GT8) (1978) 1075–1090.
[15] F. McKenna, G.L. Fenves, The OpenSees Command Language Manual, Version 1.2, Pacific Earthquake Engineering Research Center, University of California at Berkeley, 2001. <http://opensees.berkeley.edu>.
[16] Y. Zhang, J.P. Conte, Z. Yang, A. Elgamal, J. Bielak, G. Acero, Two-dimensional nonlinear earthquake response analysis of a bridge-foundation-ground system, Earthquake Spectra 24 (2) (2008) 343–386.
[17] A. Elgamal, L. Yan, Z. Yang, J.P. Conte, Three-dimensional seismic response of Humboldt Bay bridge-foundation-ground system, J. Struct. Engrg., ASCE 134 (7) (2008) 1165–1176.
[18] Z. Yang, Numerical modeling of earthquake site response including dilation and liquefaction, Ph.D. Dissertation, Department of Civil Engineering and Engineering Mechanics, Columbia University, New York, 2000.
[19] A. Elgamal, Z. Yang, E. Parra, A. Ragheb, Modeling of cyclic mobility in saturated cohesionless soils, Int. J. Plasticity 19 (2003) 883–905.
[20] A. Der Kiureghian, T. Haukaas, K. Fujimura, Structural reliability software at the University of California, Berkeley, Struct. Safety 28 (2006) 44–67.
[21] T. Haukaas, A. Der Kiureghian, Methods and object-oriented software for FE reliability and sensitivity analysis with application to a bridge structure, ASCE J. Comput. Civil Engrg. 21 (3) (2007) 151–163.
[22] M.H. Scott, T. Haukaas, Software framework for parameter updating and finite element response sensitivity analysis, J. Comput. Civil Engrg. 22 (5) (2008) 281–291.
[23] W.F. Chen, E. Mizuno, Nonlinear Analysis in Soil Mechanics: Theory and Implementation, Elsevier, Amsterdam, 1990.
[24] J.H. Prevost, A.M. Abdel-Ghaffar, A. Elgamal, Nonlinear hysteretic dynamic response of soil systems, J. Engrg. Mech. Div., ASCE 111 (EM5) (1985) 696–713.
[25] A.M. Abdel-Ghaffar, A. Elgamal, Elasto-plastic earthquake-response of 3-D non-homogeneous earth dams: theory, J. Geotech. Engrg. Div., ASCE 113 (GT11) (1987) 1293–1308.
[26] A. Elgamal, A.M. Abdel-Ghaffar, Elasto-plastic seismic-response of 3-D earth dams: application, J. Geotech. Engrg. Div., ASCE 113 (GT11) (1987) 1309–1325.

[27] A. Elgamal, Three dimensional seismic analysis of La Villita dam, J. Geotech. Engrg. Div., ASCE 118 (GT12) (1992) 1937–1958.
[28] A. Elgamal, V. Gunturi, Dynamic behavior and seismic response of El Infiernillo dam, J. Earthquake Engrg. Struct. Dyn. 22 (8) (1993) 665–684.
[29] A. Elgamal, M. Zeghal, E. Parra, R. Gunturi, H.T. Tang, J.C. Stepp, Identification and modeling of earthquake ground response: site amplification, Soil Dyn. Earthquake Engrg. 15 (1996) 499–522.
[30] Q. Gu, J.P. Conte, Z. Yang, A. Elgamal, Consistent tangent operator for multi-yield-surface J_2 plasticity material model, Int. J. Numer. Methods Engrg., submitted for publication.
[31] R.L. Kondner, Hyperbolic stress–strain response: cohesive soils, J. Soil Mech. Found. Div., ASCE 89 (SM1) (1963) 115–143.
[32] Z. Yang, A. Elgamal, E. Parra, Computational model for cyclic mobility and associated shear deformation, J. Geotech. Geoenviron. Engrg. 129 (12) (2003).
[33] Q. Gu, Finite element response sensitivity and reliability analysis of soil–foundation–structure-interaction systems, Ph.D. Dissertation, Department of Structural Engineering, University of California, San Diego, 2008.
[34] M. Barbato, A. Zona, J.P. Conte, Finite element response sensitivity analysis using three-field mixed formulation: general theory and application to frame structures, Int. J. Numer. Methods Engrg. 69 (1) (2007) 114–161.
[35] A.K. Chopra, Dynamics of Structures: Theory and Applications to Earthquake Engineering, third ed., Prentice Hall, Upper Saddle River, New Jersey, 2007.
[36] J.C. Simo, T.J.R. Hughes, Computational Inelasticity, Springer-Verlag, New York, 1998.
[37] R.T. Haftka, Z. Gurdal, Elements of Structural Optimization, third ed., Kluwer Academic Publishers, 1993.